Hard - X-rays selected Active Galactic Nuclei. I. A radio view at high-frequencies

E. Chiaraluce,[1,2]⋆ F. Panessa,[1] G. Bruni,[1] R. D. Baldi,[3,4,1] E. Behar,[5] F. Vagnetti,[2] F. Tombesi,[2,6,7,8] I. McHardy[3]

[1]*INAF - Istituto di Astrofisica e Planetologia Spaziali, via del Fosso del Caveliere 100, I-00133 Roma, Italy*
[2]*Dipartimento di Fisica, Univerisità di Roma Tor Vergata, via della Ricerca Scientifica 1, I-00133 Roma, Italy*
[3]*Department of Physics & Astronomy, University of Southampton, Hampshire SO17 1BJ, Southampton, United Kingdom*
[4]*Dipartimento di Fisica, Universitá degli Studi di Torino, via Pietro Giuria 1, 10125 Torino, Italy*
[5]*Physics Department, Technion, Haifa 32000, Israel*
[6]*INAF Astronomical Observatory of Rome, Via Frascati 33, 00078 Monteporzio Catone, Italy*
[7]*Department of Astronomy, University of Maryland, College Park, MD 20742, USA*
[8]*NASA/Goddard Space Flight Center, Code 662, Greenbelt, MD 20771, USA*

ABSTRACT

A thorough study of radio emission in Active Galactic Nuclei (AGN) is of fundamental importance to understand the physical mechanisms responsible for the emission and the interplay between accretion and ejection processes. High frequency radio observations can target the nuclear contribution of smaller emitting regions and are less affected by absorption. We present JVLA 22 and 45 GHz observations of 16 nearby ($0.003 \leq z \leq 0.3$) hard - X-rays selected AGN at the (sub)-kpc scale with tens μJy beam^{-1} sensitivity. We detected 15/16 sources, with flux densities ranging from hundreds μJy to tens Jy (specific luminosities from $\sim 10^{20}$ to $\sim 10^{25}$ $W\,Hz^{-1}$ at 22 GHz). All detected sources host a compact core, with 8 being core-dominated at either frequencies, the others exhibiting also extended structures. Spectral indices range from steep to flat/inverted. We interpret this evidence as either due to a core+jet system (6/15), a core accompanied by surrounding star formation (1/15), to a jet oriented close to the line of sight (3/15), to emission from a corona or the base of a jet (1/15), although there might be degeneracies between different processes. Four sources require more data to shed light on their nature. We conclude that, at these frequencies, extended, optically-thin components are present together with the flat-spectrum core. The $L_R/L_X \sim 10^{-5}$ relation is roughly followed, indicating a possible contribution to radio emission from a hot corona. A weakly significant correlation between radio core (22 and 45 GHz) and X-rays luminosities is discussed in the light of an accretion-ejection framework.

Key words: techniques: interferometric - galaxies: active - galaxies: nuclei - galaxies : Seyfert - radio continuum: galaxies - X-rays: galaxies.

1 INTRODUCTION

Active Galactic Nuclei (AGN) show a large variety of radio morphologies, with sources exhibiting compact cores, jets, lobes and knots in radio images, in a wide range of strengths and on scales ranging from sub-pc up to kpc and even Mpc scales. A deep knowledge of the origin of radio emission in AGN is of fundamental importance in order to

understand the physics of accretion and ejection onto supermassive black holes (SMBHs), as well as the feedback mechanisms that jets and outflows are thought to produce on the host galaxy.

From a radio perspective, AGN are historically divided into Radio Loud (RL) and Radio Quiet (RQ) based on the value of the parameter R=$\log \frac{f(4400\text{Å})}{f(6\,cm)}$, which gives a measure of the strength of radio emission relative to the optical one, with RL objects having R>1 and RQ having R<1

⋆ elia.chiaraluce@inaf.it

(Kellermann et al. 1989)[1]. Recently, Padovani (2016) proposed a distinction between jetted (with a strong, relativistic jet) and non jetted AGN. However, by adopting this definition caution should be paid as there are examples of relatively low power radio sources with a clear jet like structure, even though not relativistic. For the sake of clarity, we maintain the RL/RQ classification in this work.

While the origin of radio emission in RL AGN, which represent only a minority of the overall population (∼10 per cent), has been identified as synchrotron radiation from relativistic jets (e.g. Begelman et al. 1984), the origin of radio emission in RQ objects is still matter of debate, see Panessa et al. (2019) for a review of the emission mechanisms which may be at work in RQ AGN. There is increasing evidence that RQ are not necessarily radio silent (e.g. Nagar et al. 2002), indeed they emit in the radio, although at lower levels (e.g. Ho & Ulvestad 2001), and they can be associated with outflowing phenomena like jets, but probably less powerful, less collimated and sub-relativistic (e.g. Middelberg et al. 2004; Giroletti & Panessa 2009). However, a complete and systematic census of the radio properties of the AGN population is still missing.

Most of the surveys performed so far comprising RQ objects had suffered from observational biases and were mainly focused on Low-Luminosity AGN (LLAGN), category comprising both low-luminosity Seyferts and LINERs, where radio emission is expected to be ubiquitous (Ho & Ulvestad 2001; Nagar et al. 2002). Indeed, these objects would be characterised by a radiatively inefficient accretion flow (as an ADAF, see Narayan & Yi 1994) which would favour the fuelling and launching of collimated outflows/jets, resulting in detectable radio emission; while in Seyferts and quasars at higher accretion rates (but other parameters are thought to be involved, such as black hole mass and spin), the radiative output of the AGN would be dominated by the emission from a standard optically-thick and geometrically-thin accretion disk extending down to the innermost regions of the accretion flow (see review of Heckman & Best 2014).

A tight correlation between the radio and X-rays luminosities has been established for RQ AGN (e.g. Brinkmann et al. 2000; Salvato et al. 2004; Panessa et al. 2007, 2015; Chiaraluce et al. 2019), suggesting a physical connection between the emitting regions. The scaling of this relationship with the black hole mass has led to the formulation of the "black hole fundamental plane" where some classes of active black holes have been unified under the same physics (Merloni et al. 2003). In particular, LLAGN, similarly to "hard state" X-rays Binaries (XRB), seem to follow an inefficient accretion track (Falcke et al. 2004), while highly accreting AGN, as well as "outliers" hard-state XRBs (e.g. Dong et al. 2014), follow an efficient accretion track (see Figure 7 in Coriat et al. 2011). In XRB, the transition between the accretion states (i.e. the hysteresis diagram) is believed to be due not only to the accretion rate (e.g. Maccarone 2003), but also on other fundamental physical quantities, like the disk magnetic field (Petrucci et al. 2008; Begelman & Armitage 2014), see (e.g. Fender & Belloni 2012) for the open issues

related to this subject. In AGN there may be as well transitions between one mode and another (see for instance the class of changing look AGN), with some common features with XRB, and still matter of speculation (e.g Heckman & Best 2014).

Extensive studies have been carried out on LLAGN (e.g. Ho & Ulvestad 2001; Giroletti & Panessa 2009; Baldi et al. 2018) as well as on more luminous objects, like the PG quasar sample, comprising relatively nearby (z≤0.5) high-Eddington objects (e.g. Kellermann et al. 1989; Kukula et al. 1998). Interestingly, these works have led to generally high detection rates. In both cases, a variety of properties has been reported, with some sources exhibiting compact morphologies, accompanied by jet-like features, which remain compact down to mas scales; the high-brightness temperature and flat-spectrum have led to an interpretation in terms of emission raising from the optically-thick base of a jet; other sources exhibit elongated components, double and triple structures, multiple components as well as rings of radio emission, with spectral indices ranging from steep to flat/inverted (e.g. Kukula et al. 1995a; Barvainis et al. 1996; Kellermann et al. 1994; Leipski et al. 2006; Ho & Ulvestad 2001; Orienti & Prieto 2010; Panessa & Giroletti 2013; Baldi et al. 2018; Chiaraluce et al. 2019).

This evidence suggests that different physical processes might interplay in RQ AGN, like star formation, both on extended (i.e. few kpc) scale as well as on unresolved (i.e. sub-kpc) scale (e.g. Zakamska et al. 2016; Smith et al. 2016), typically associated to a steep GHz spectrum; emission from accretion disc winds in the form of either synchrotron emission from shocks or free-free emission (e.g. Blustin & Fabian 2009; Nims et al. 2015); emission from a compact, flat spectrum opaque synchrotron source interpreted as the base of a jet (e.g. Falcke & Biermann 1995).

Since recently, the finding that highly accreting RQ AGN follow the Güdel-Benz relation (Guedel & Benz 1993), i.e. $L_R/L_X \sim 10^{-5}$, valid for coronally active stars, has led to the formulation of coronal models for RQ AGN, in which both radio and X-rays emission would come from a compact corona (e.g. Laor & Behar 2008). In this picture, several authors reported the finding of a high frequency (i.e.≤95 GHz) excess emission with respect to the extrapolation from the low-frequency (steeper) spectrum (e.g. Baldi et al. 2015; Behar et al. 2015; Doi & Inoue 2016). This evidence has been interpreted as signature of the emission from a compact, optically-thick, flat-spectrum component, which dominates in the mm range. This component is recognised to be a corona which is heated through magnetic reconnection events (e.g. Raginski & Laor 2016).

High-frequency radio observations are particularly useful to target the nuclear contribution of the AGN, eventually testing the emergence of a compact, flat/inverted-spectrum, optically-thick core; indeed radio emission from extended, optically-thin, steep spectrum regions, which may not be directly AGN related, is expected to be resolved out at these frequencies. Moreover, the high frequency approach allows us to characterise the nuclear radio emission of our sources in a frequency regime where smaller regions of emission can be probed due to the improving angular resolution with frequency and in which absorption mechanisms like synchrotron self absorption and free-free absorption are less effective (e.g. Kellermann 1966; Park et al.

---

[1] Terashima & Wilson (2003) proposed a definition based on the ratio $R_X = \log \frac{\nu L_\nu (6\,cm)}{L_{2-10\,keV}}$, with a -4.5 threshold between the two classes.

2013). Only few works have been performed at high frequencies to characterise the radio emission in RQ AGN, one of them being the 1-arcsec, 22 GHz JVLA characterisation of 100 RQ Swift/BAT AGN (0.003≤z≤0.049) survey performed by Smith et al. (2016, 2020). Various morphologies were found, from compact (~half of the sample), to extended, interpreted as due to star formation, and jet-like, with flux densities in agreement with both scale-invariant jet models and coronal models. Park et al. (2013) reports single-dish observations for 305 relatively nearby AGN (0.01≤z≤0.06) at 22 and 43 GHz, obtained from the cross match of Sloan Digital Sky Survey Data Release SDSS-DR7[2] and FIRST[3] (although the sample contains both LINERs and Seyferts). They found a prevalence of flat/inverted spectra, with however lower detection rates with respect to previous works (i.e. 37 and 22 per cent at 22 and 43 GHz, respectively).

Our strategy is to characterise the high-frequency radio emission of a sample of hard-X-rays selected AGN spanning a wide range of radio-loudness (see right panel of Fig. 1) with Jansky Very Large Array (JVLA) observations in C-configuration, which guarantees us a 1-arcsec resolution, that translates in scales of $\leq$ kpc. With respect to previous works (e.g. Smith et al. 2016, 2020), our novel approach consists in the use of dual frequency observations at 22 and 45 GHz, which allow us to derive high-frequency spectral indices and provide stronger constraints in the discrimination between the diverse radiative processes responsible for the observed radio emission. The hard-X-rays selection of the sample makes it relatively free of selection biases with respect to other wavebands (see discussion in Ho & Ulvestad 2001), giving us the opportunity to have an unbiased view of the radio population. Moreover, our sample of nearby (0.0033≤z≤0.323) AGN covers, with respect to LLAGN samples and the PG quasar sample, an intermediate range of Eddington ratios ($L_{Bol}/L_{Edd} \geq 10^{-3}$), which enable us to characterise the intermediate accretion regime, for the morphology and energetics study, to compute simultaneous high-frequency spectral indices and test the possible physical scenarios.

This work is part of a larger and comprehensive project aimed at characterising the properties of our hard X-ray selected sample in a wide frequency range, studying the core and extended emission energetics, and the morphology of the radio emission at different frequencies. In a forthcoming work (Chiaraluce et al. in prep), we will couple the high-frequency observations with low-frequency data (C, X and Ku bands, VLA project 19A-018, PI: Chiaraluce). This will enable us to build radio spectral indices and spectral energy distributions (SED), in relation to multi-band data (X-ray, optical, infrared) to derive fundamental parameters on the accretion in light of recent models. Moreover, we have been awarded dual-frequency (3.6 and 6 cm) VLBI observations for 32/44 sources in the sample in a large program of the European VLBI Network (EVN) (code:EC070, 74 hrs). This observations will allow us to spread light on the pc-scale emission of the sources, to break the degeneracy between different physical processes and obtain brightness tempera-

Table 1. The 16 sources considered in this work. *Columns:* (1) Target name; (2) & (3) J2000 positions; (4) Masetti's optical classification. Columns (2)-(5) are from Malizia et al. (2009).

Name	RA (J2000)	Dec (J2000)	Seyfert Type	z
(1)	(2)	(3)	(4)	(5)
IGRJ00333+6122	00 33 18.41	+61 27 43.1	S1.5	0.105
NGC788	02 01 06.40	−06 48 56.0	S2	0.0136
NGC1068	02 42 40.71	−00 00 47.8	S2	0.0038
QSOB0241+62	02 44 40.71	+62 28 06.5	S1	0.044
NGC1142	02 55 12.19	−00 11 02.3	S2	0.0288
B30309+411B	03 13 01.96	+41 20 01.2	S1	0.136
NGC1275	03 19 48.16	+41 30 42.1	S2	0.0175
LEDA168563	04 52 04.85	+49 32 43.7	S1	0.029
4U0517+17	05 10 45.51	+16 29 55.8	S1.5	0.0179
MCG+08-11-11	05 54 53.61	+46 26 21.6	S1.5	0.0205
Mkn3	06 15 36.36	+71 02 15.1	S2	0.0135
Mkn6	06 52 12.25	+74 25 37.5	S1.5	0.0188
NGC4151	12 10 32.58	+39 24 20.6	S1.5	0.0033
NGC4388	12 25 46.75	+12 39 43.5	S2	0.0084
NGC5252	13 38 16.00	+04 32 32.5	S2	0.023
IGRJ16426+6536	16 43 04.70	+65 32 50.9	NLS1	0.323

ture estimates, useful to discriminate between thermal and non-thermal radiative processes.

In this paper we use a flat Λ-CDM cosmological model with following parameters: H_o=70 km s^{-1} Mpc^{-1}, Ω_m=0.3 and Ω_{Λ}=0.7 (Jarosik et al. 2011).

2 SAMPLE

The starting point of our work is the sample of 140 extra galactic objects observed by INTEGRAL/*Imager on Board the Integral Satellite* in the 20 – 40 keV range (Bird et al. 2007). The IBIS survey comprises sources at energies ≥20 keV with a sensitivity of ~8×10^{-11} $erg\ s^{-1}\ cm^{-2}$. Malizia et al. (2009) applied a Schmitt V/V$_{max}$ test to the IBIS AGN with a significance threshold of ~5 sigma, obtaining a sample of 88 AGN, which comprises 41 Seyfert-1 objects, 5 Narrow-line Seyfert 1 (NLS1), 33 Seyfert-2 and 9 Blazars[4]. This sample has several advantages: it is statistically complete and, being hard X-ray selected, it is relatively free of common selection biases affecting samples selected in other ways, like UV-excess and IR (see discussion in Ho & Ulvestad 2001). It has also a wide coverage on information at multifrequencies, particularly at X-rays, as it has been the subject of several studies (e.g. Panessa et al. 2016, 2015; Malizia et al. 2014; Molina et al. 2013; de Rosa et al. 2012; Panessa et al. 2011). Moreover, it represents mainly relatively high luminosity (41.5 < log $L_{2-10 keV}(ergs^{-1})$ < 44.5) and highly accreting ($L_{bol}/L_{Edd} \geq 10^{-3}$) AGN, with a wide range of X-ray radio loudness R$_X$ parameter values (-6.5 ≤ R$_X$ ≤-0.5).

Considering only the non-blazars objects in the sample (79 out of 88), Panessa et al. (2015) have performed a 1.4 GHz radio characterisation of the 79 AGN with the NRAO Very Large Array Sky Survey (NVSS, Condon et al. 1998) and the Sydney University Molonglo Sky Survey (SUMSS, Bock et al. 1999; Mauch et al. 2003), having a matched angular resolution of ~45 arcsec and RMS of ~0.45 and 1 mJy beam^{-1} for the NVSS and SUMSS, respectively. They obtained a high detection rate (~89 percent), with a variety of

---

[2] Sloan Digital Sky Survey Data Release Seventh
[3] Faint Image of Radio Sky at Twenty cm

[4] We refer to the optical classification by Masetti, `http://www.iasfbo.inaf.it/~masetti/IGR/main.html`, but see also Masetti et al. (2012)

radio morphologies: unresolved, slightly resolved, on scales from few up to hundreds kpc, exhibiting jet-like features and double/triple structures, as well as diffuse emission. They have also found a significant correlation between the radio luminosity and the X-rays luminosity (either the 2-10 keV or the 20-100 keV one), which have been interpreted as a symptom of an efficient underlying accretion physics, in analogy with 'outliers' hard-state XRBs.

In this picture, our group has started a wide-band radio characterisation with the Karl G. Jansky Very Large Array (JVLA) for the part of visible sources in our sample, i.e. north of -30 deg in declination (44 out of 89), with a separate characterisation at high frequencies (i.e. 22 and 45 GHz) and low frequencies (i.e. 5, 10 and 15 Ghz), matched in resolution thanks to the different requested JVLA configurations (C and B, respectively).

In this work, we report observations for 16 objects out of 44 (see Table 1) which have been observed by the JVLA at the high frequencies K and Q (22 and 45 GHz, respectively, VLA project 18B-163) in C configuration (see Table 1). The reason for which only 16/44 sources have been observed is because these sources could be observed in the VLA LST range 0 - 12, in which the scheduling pressure (i.e. the number of sessions desiring per hour) is lower[5] . In Fig. 1 we show the distribution of redshifts, Eddington ratios and radio-loudness parameter for the full sample of 44 objects at DEC > -30 deg (which we will call the 'Parent' sample) and for the objects considered in this work ('Reference' sample). A Kolmogorov-Smirnov test performed considering the three aforementioned quantities to compare the parent and the reference sample results, in all the three cases, in a high (P > 0.7) p-value, suggesting that the null hypothesis that the two samples are drawn from the same parent population cannot be rejected, suggesting that the Reference sample represents the physical properties of the Parent sample.

Considering the radio loudness of our sources, we have computed the optical radio loudness parameter R for the 16 sources in our sample, either using archival 5 GHz flux measurements, when available, or extrapolating the flux density at 5 GHz from the 22 GHz one, with the 22−45 GHz spectral index from our observations (see following sections). We have found that 8 sources can be classified as RL, i.e. IGRJ00333+6122, NGC1068, QSOB0241+62, B30309+411B, NGC1275, LEDA168563, MCG+08-11-11 and Mkn6. However, we caution that a distinction between RL and RQ objects based on the value of the radio-loudness parameter may result in an incorrect and incomplete picture about the strength of radio emission relatively to other bands, both because of systematics, as the B flux being dominated by host galaxy in obscured type 2 objects (e.g. Padovani 2016) and, as noted before, because it may not take into account ejection phenomena of various morphologies and strengths, which have been observed in objects traditionally classified as RQ.

3 OBSERVATIONS AND DATA REDUCTION

A total of ~2.2 hrs of Time-On-Source has been collected across 4 observing runs in the period November - December 2018. In Table 2 we list our targets, together with the observing date and the calibrators, grouped by observing block.

Each source has been observed at two frequencies: 22 and 44 GHz, corresponding to the K and Q bands. The observing bandwidths for the two frequencies were 8 GHz, and all bands were subdivided into 64 spectral windows (spw) of 128 MHz bandwidth, and each spw were subdivided into 64 channels. In Table 2 we indicate the sources with corresponding Time-On-Source at each band and the theoretical RMS achievable. The observation of each source has been bracketed between the observations of a nearby phase calibrator, chosen as the nearest one in a radius of 10 degrees, for at least a minute. At the high-frequencies the main responsible for phase fluctuations is the troposphere, and when the Time-On-Source was too large to exceed the recommended cycle time (which ensures a good phase-tracking), we decided to split it into two or more scans on the source, in order to perform a good phase calibration. The absolute flux density calibrator, for each group, has been observed for a total of 7m 30s at the beginning or ending of the block.

In order to reduce and calibrate our data we used the Common Astronomy Software Application (CASA 5.4.1 version[6], McMullin et al. 2007). The full raw datasets were downloaded from the NRAO science data archive[7] as SDM-BDF datasets with flags generated during the observations applied. The calibration has been performed via the CASA pipeline of the same version. After calibration, the plots were inspected for residual RFI and the two bands were split into separate ms files.

Initially, the imaging strategy for the two frequencies has been the following. We considered the deconvolution algorithm of Högbom (1974) in TCLEAN with image size of 1024 pixels, with cell sizes of 0.14 and 0.08 arcsec per pixel for the K and Q bands, respectively, which correspond to roughly 1/6 of the beam size for both frequencies. In the two frequency bands the initial weighting algorithm used has been the Briggs (1995) algorithm with robustness parameter equal to 0.5, which ensures a balance between resolution and sensitivity. However, in order to correctly derive the spectral index between the K and Q bands, we also computed tapered radio maps at the Q band, in order to have a matched resolution, with a natural weighting algorithm, in order to give more weight to the short baselines. In this way the observations have an approximately equal UV coverage in wavelengths, and the spectral index is calculated by comparing flux densities obtained from the same emitting regions: this is important for sources exhibiting diffuse, resolved morphology, as it may otherwise led to an artificial steepening of the spectral index.

For sources presenting imaging artifacts, we first inspected the calibrated visibilities plots in search of unflagged RFI signatures, which we eventually manually flagged. Then, in order to remove the artifacts and enhance the

---
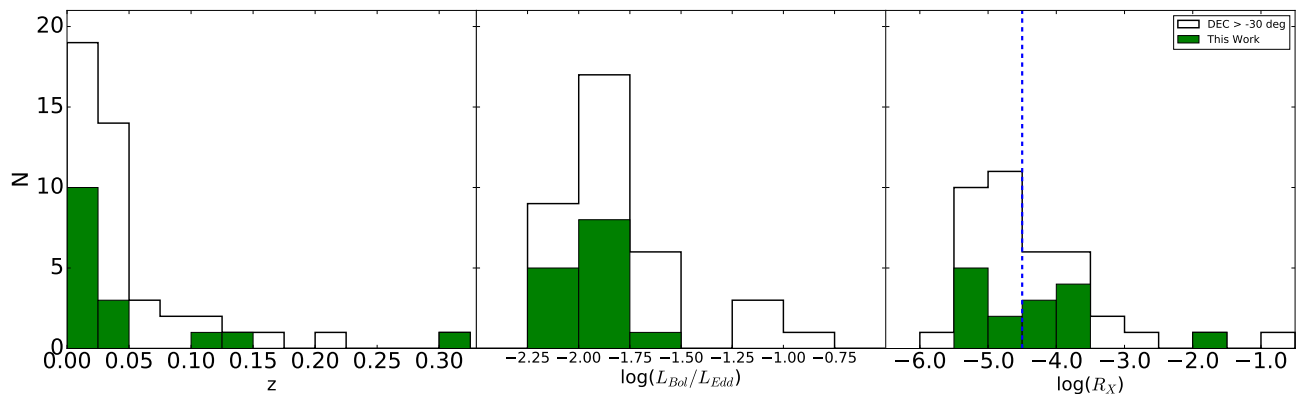
Figure 1. Histogram showing the distribution of redshift (from Malizia et al. 2009, left panel), Eddington ratio (L_{Bol}/L_{Edd}, centre panel) and radio-loudness parameter (from quantities tabulated in Panessa et al. 2015, right panel) for the parent sample (DEC > -30 deg, semi-filled histogram) and for the sources considered in this work (green). The blue, vertical dashed line is the R_X = -4.5 limit of Terashima & Wilson (2003).

signal-to-noise ratio of the maps we performed a self-calibration, as our sources are bright enough to allow such a procedure. Typically, two cycles of phase-only self calibration were enough to remove the artifacts, but in some cases the two phase-only steps were followed by a phase-amplitude self calibration, which led to the final maps.

For the phase calibrators and absolute flux density calibrators, the same imaging technique as before has been applied. In the case of flux calibrators, we measured the integrated flux densities via a gaussian elliptical fitting on the image plane as performed by the CASA IMFIT and we compared the results with modelled flux densities quoted by Perley & Butler (2017). All the measured flux densities have been found to agree within the 5 per cent with tabulated flux densities, so we adopt an average 5 per cent flux calibration error. The positional accuracy of the phase calibrators is order of few mas, therefore the estimates of radio positions are dominated by uncertainty in the determination of the peak of the gaussian fit as performed by IMFIT. The positions, peak intensities, integrated flux densities, deconvolved sizes and position angle (PA) of the sources were estimated by fitting a two-dimensional single or multiple Gaussian in the image plane via the CASA task IMFIT. We determined the rms noise of each map from a source-free annular region around the source. The uncertainties in the final flux density measurements are affected by fitting errors from IMFIT, and flux calibration error of 5 per cent, which are added in quadrature and adopted as the error measurements. The positional accuracy of the detected radio components is limited by the positional accuracy of the phase calibrators, typically few mas, and by the accuracy of the gaussian fit to the source brightness distribution as performed by IMFIT. Therefore, the uncertainty on radio position expressed in this work is the sum in quadrature of the two contributions. In cases in which the morphology is resolved and in which a multiple gaussian fit is not appropriate, the parameters associated to the emitting components have been estimated using interactively defined boundaries via the CASA task VIEWER. The uncertainties associated to the peak and integrated flux densities are given by the formula $\sigma_S = \sqrt{N \times (rms)^2 + (0.05 \times S)^2}$, where N is the number of beam areas covered by a source of flux density S, and it is taken into account an uncertainty

of 5 per cent in the absolute flux density scale (see Ho & Ulvestad 2001).

In Table A1 we summarise our imaging results, and in Figs. A1 - A4 we show the coloured and contour maps of the detected sources.

4 RESULTS

4.1 Detection rates

We define a source as detected if the peak intensity is above $\geq 5\ \sigma$, where σ is the image RMS. However, a source exhibiting a peak intensity $3 \leq S_P \leq 5\ \sigma$ is defined as marginal detection, following the same criterion in Ho & Ulvestad (2001).

Our strategy results in a high detection rate, with 15 out of 16 sources detected, which results in a detection rate of 89±16 per cent [8]. The majority of the sources are detected with a high significance (S≫10σ), only two sources, namely NGC 788 and IGR J00333+6122, are detected with a significance in between 5σ and 10σ.

The detection rate obtained for our hard-X-rays selected sample is higher with respect to results obtained at lower frequencies for both LLAGN (e.g. Ho & Ulvestad 2001) and brighter RQ AGN (e.g. Kellermann et al. 1989; Kukula et al. 1998), also at higher frequencies. Indeed, in the mm-range (i.e. $\nu \geq 95$ GHz) Behar et al. (2018) found a detection rate of ~77 per cent for a sample of highly-accreting AGN (see also Doi et al. 2011, for the LLAGN in the mm range). Our result confirms a trend which have been observed at these frequecies by Smith et al. (2020) for 100 low-redshift AGN selected at 14-195 keV from the Swift-BAT, 96 per cent, however it is not in agreement with the lower detection rates found by Park et al. (2013) with single dish measurements at 22 and 43 GHz (37 and 22 per cent, respectively).

---

[8] Given the small statistics of our sample, a meaningful way of giving a detection rate is via the Laplace point estimate formula (Laplace 1812), which in our case give us a detection rate of 89 per cent for the full sample, with an associated uncertainty which can be estimated via the Adjusted Wald method (e.g. Sauro & Lewis 2005) as half the Confidence Intervals.

Table 2. List of calibrators (flux and phase) per observation group. *Columns:* (1) Target name; (2) Observation date; (3) Absolute flux density scale calibrator; (4) Phase Calibrator; (5) Observing time in K band for the science target; (6) expected (theoretical) RMS in K band; (7) Observing time in Q band for the science target; (8) expected (theoretical) RMS in Q band.

		Calibrators					
Target	Obs Date (dd/mm/yy)	Flux	Phase	Time (s)	σ_{th} (μJy beam^{-1})	Time (s)	σ_{th} (μJy beam^{-1})
(1)	(2)	(3)	(4)	(5)	(6)	(7)	(8)
NGC788	21/11/18	3C138	J0209-0438	90	25	300	39
NGC1068	21/11/18	3C138	J0217+0144	90	25	320	38
NGC1142	21/11/18	3C138	J0312+0133	898	8	300	39
4U0517+17	21/11/18	3C138	J0510+1800	90	25	300	39
IGRJ00333+6122	21/11/18	3C147	J0109+6133	125	26	310	39
B30309+411B	21/11/18	3C147	Self-cal	95	25	125	61
LEDA168563	21/11/18	3C147	J0533+4822	140	21	349	36
NGC4151	21/11/118	3C286	J1206+3941	90	25	300	39
IGRJ16426+6536	21/11/118	3C286	J1645+6330	858	8	300	39
QSOB0241+62	02/12/18	3C147	Self-cal	60	30	90	72
NGC1275	02/12/18	3C147	Self-cal	60	30	90	72
MCG+08-11-11	16/12/18	3C147	J0607+4739	90	25	329	37
Mkn3	16/12/18	3C147	J0524+7034	150	20	170	52
Mkn6	16/12/18	3C147	J0714+7408	90	25	300	39
NGC4388	21/12/18	3C286	J1218+1105	900	8	300	39
NGC5252	21/12/18	3C286	J1405+0415	90	25	120	62

One source in our sample, i.e. IGR J16426+6536, has not been detected, and we provide 3-sigma upper limits of 24 and 162 μJy beam^{-1} at K and Q bands, respectively, corresponding to radio powers of $\sim 6 \times 10^{20}$ and $\sim 3 \times 10^{21}$ $W\,Hz^{-1}$) at the two frequencies. This source is classified as Narrow Line Seyfert 1 (NLS1) and was neither detected in the NVSS survey (Panessa et al. 2015, upper limit on peak intensity of 1.2 mJy).

4.2 Flux densities and luminosities

The radio flux densities of the detected sources (indicated in Table A1), range from hundreds of μJy for the faintest ones, i.e. IGR J00333+6122 and NGC 788, to tens of mJy, which translates into radio luminosities in the range of $37 \leq log\nu L_\nu(ergs^{-1}) \leq 40$.

Considering RL sources, three of them exhibit significantly higher radio flux densities at both frequencies with respect to all the other sources (see Fig. 3).

For these three sources, the measured flux densities range from hundreds of mJy (QSO B0241+62), to few Jy (B3 0309+411B) up to tens of Jy (NGC 1275). These sources are known to be powerful radio sources (e.g. Lister et al. 1994; Healey et al. 2007; Bruni et al. 2019), and a simple comparison with previous works is not straightforward as, besides the variety of resolutions, sensitivities and frequency bands used, the flux densities in literature may be affected by radio variability. Indeed, B3 0309+411 is known for having a variable core flux density (e.g. Konar et al. 2004, at 1.4 and 5 GHz) and NGC 1275 is an example of recurrent jet activity (e.g. Nagai et al. 2010), therefore our flux densities embed the variable contribution of multiple sub-kpc components. For the rest of RL (5/8) and RQ sources there are no significant differences in the flux densities, which range from hundreds of μJy up to tens of mJy, with some extended components of resolved sources up to few hundreds of mJy.

These flux densities are in agreement with previous surveys performed at comparable resolution and sensitivities with the VLA, although most at lower frequencies (e.g. Kellermann et al. 1989; Barvainis et al. 1996; Kukula et al. 1998; Leipski et al. 2006), and with works performed in the same frequency coverage and with samples with similar characteristics, as Park et al. (2013) and Smith et al. (2020). Our flux densities are also in agreement with 3-mm CARMA flux densities derived by Behar et al. (2018) for 26 hard-X-rays selected AGN from Swift-BAT. If we consider NGC 4388, then the flux of the core component, 3.6±0.3 mJy, is compatible with our estimate at 22 GHz.

4.3 Morphology and spectral indices

Our dual frequency approach at high frequency allows us to take a step forward in the state-of-the-art and compute high-frequency spectral indices and test the occurrence of compact versus jet-like features in a sample of hard-X-rays selected AGN.

We define a spectral index as $S_\nu^I \propto \nu^{-\alpha}$, where S_ν^I is the integrated flux density. In Table A1 we report the spectral indices for all the detected sources and components, in which the spectral index has been calculated considering the integrated flux density measured in K - band maps and in the naturally-weighted, tapered Q - band maps, in order to have matched resolutions. The uncertainties associated to the spectral indices has been estimated as $\sqrt{(\sigma_{f_1}/S_{f_1})^2 + (\sigma_{f_2}/S_{f_2})^2}/ln(f_2/f_1)$, where $\sigma_{f_{1,2}}$ and $S_{f_{1,2}}$ are the uncertainties on the flux density and the flux density at the two frequencies (Ho & Ulvestad 2001), which are the central frequencies of the K and Q bands (therefore our flux densities are the mean across the bandwidth).

Considering maps in Figs. A1 - A4 and deconvolved sizes in Column (7) of Table A1, then all sources have a compact core component.

No extended emission is detected in 8 out of 16 sources

that show a core dominated morphology. Considering the redshift of the sources, this means that they are compact on linear scales smaller than, on average, ~ 1.5 kpc, i.e smaller than 2.5 kpc for the highest-redshift source, B30309+411B, while as low as ~ 70 pc for the lowest redshift one, NGC 4151. For most of our sources the spatial scales sampled by our sources ranges from hundreds of pc to tens of pc, while for two sources, namely B30309+411B and IGRJ00333+6122, the observations maps scales of order of ~ 2 kpc. We will discuss theses two cases in Section 5. The spectral indices for the compact sources range from flat/inverted to steep[9], with a prevalence of steep spectra, as also found in previous VLA studies (e.g. Kukula et al. 1998, although at lower frequencies).

The remaining 7 sources are characterised by a variety of morphologies. Three sources, namely NGC 4151, Mkn 6 and MCG +08-11-11, exhibit an elongated morphology, in the direction NE-SW, N-S and N-S, respectively. In the case of Mkn 6, the double morphology seen in the Q band map is not visible in the naturally-weighted, tapered Q-band map. Two sources, i.e. Mkn 3 and NGC 4388, display a double morphology, extending on linear scales of 810 pc (NGC 4388) and 1.1 kpc (Mkn 3) in the direction NE-SW and E-W, respectively. Two sources, NGC 1068 and NGC 1142, exhibit a complex morphology, in which multiple emitting components are visible, extending on linear scales of ~ 1.2 and ~ 11 kpc, respectively. In Table A1, for clarity, we tabulated first the information for the flux of compact sources, and then that for the resolved sources, indicating the single components.

When considering the radio loudness, no bimodality is found in the observed morphologies and spectral indices, as both RL and RQ objects tend to have both steep and flat/inverted spectra.

## 4.4 Radio-loudness and Eddington ratios

Adopting the optical radio loudness parameter, 8/16 sources result as RL AGN. However, this definition may be affected by several systematic uncertainties, for example in the case of type-2 objects, in which the B-band flux may be dominated by host galaxy emission (e.g. Padovani 2016). For this reason, we also computed the radio loudness parameter in the Terashima & Wilson (2003) definition, i.e. $R_X = L_R/L_{2-10\,keV}$, in which, instead of the 5 GHz luminosity, we used our 22 and 45 GHz core luminosities, which allow us to compare the nuclear radio emission of the cores with the nuclear X-ray luminosity. According to this, 7 sources are classified as RL, i.e. NGC1068, QSOB0241+62, B30309+411B, NGC1275, MCG+08-11-11, Mkn6 at both frequencies, NGC5252 RL only at 22 GHz, 4U0517+17 RL only at 45 GHz. In Panessa et al. (2015), a continuous distribution of values is found, with a prevalence of RQ objects. A continuous distribution of radio-loudness is found as well by Burlon et al. (2013) at 20 GHz with ATCA and BAT luminosities (although at higher values, $-4 \leq R_X \leq 0$). From the hard X-ray selection, the resulting fraction of RL AGN is

therefore higher than the 10 per cent usually found from low frequency observations (e.g. Panessa et al. 2019). It is clear that the radio loudness parameter highly varies depending on the adopted definition, therefore should not be taken as a characterising parameter for AGN. Three sources are occupying a different locus in the radio (either 22 or 45 GHz) X-rays plane with respect to the rest of sources (which comprise both RL and RQ objects, in either of the definitions). Indeed, they are know powerful radio sources and exhibit compact cores and flat/inverted spectra, which can be interpreted as due to a jet closely aligned to the line of sight.

We can investigate the relation between the derived physical properties of our sample, i.e. radio 22 and 45 GHz core peak luminosities and spectral index, and relevant physical quantities of the black hole like the Eddington ratio and the black-hole mass, indicated in Table 3. In order to calculate the Eddington ratio, we used the recipe in Lusso et al. (2012) (see their Table 3), in particular the formula $L/L_{Edd} = q/[(L_X/L_{Edd})^{-1} - m]$, where m and q are two parameters which have different values depending on whether the object is a type 1 or 2. The X-ray luminosities are from Panessa et al. (2015), and are absorption corrected. In order to calculate the Eddington luminosities, we have compiled BH masses from literature. The most reliable methods for the determination of the black hole mass are via reverberation mapping measurements (e.g. Peterson 2003; McLure & Jarvis 2002), and by considering the spatially resolved kinematics of stars or gas in close proximity to the black hole (e.g. Ferrarese & Ford 2005; Yong et al. 2016), but both methods are limited by the statistics of objects studied. Another method which results in the most precise estimates of the black hole mass is via masers measurements (e.g. Greene et al. 2016). Only in four sources, namely NGC4388, Mrk3, NGC1275 and NGC1068, maser emission has been detected, but only for NGC4388 and NGC1068 mass estimated from masers are available, and we report them in Table 3. When masses from above measurements were not available, values calculated from other methods have been considered, as using the relations between the black hole mass and the stellar velocity dispersion and bulge luminosity (e.g. Ferrarese & Merritt 2000; Magorrian et al. 1998). Typical uncertainties range from 0.3 dex to 0.7 dex (see References in Table 3).

We did not find significant trend of our high frequency core spectral indices with either the Eddington ratio or the black hole mass (see Fig. 2), as instead found by Laor et al. (2019) for a number of PG quasars at lower frequencies (5 - 8 GHz), in which they isolated the core component considering highest resolution VLA observations. They have found a trend according to which high Eddington sources would favour the production of outflows, which would be associated with optically-thin spectral slopes, while in low Eddington ratio object the launching of outflows is quenched and only the compact, flat-spectrum core would be present present, probably of coronal origin. We interpret this discrepancy as first due to a limited statistic, and second to the fact that the emission processes and regions involved at high frequency might be different with respect to lower frequencies. If we compare high frequency spectral slopes with that in literature at lower frequencies at same resolution, we find a general agreement. However, the presence of multiple components found at high frequency makes it difficult unam-

---

[9] We define a steep spectrum as having $\alpha \geq 0.5$, and a flat one as having $\alpha < 0.5$, as in Panessa & Giroletti (2013). We define a spectrum as inverted if $\alpha < 0$.
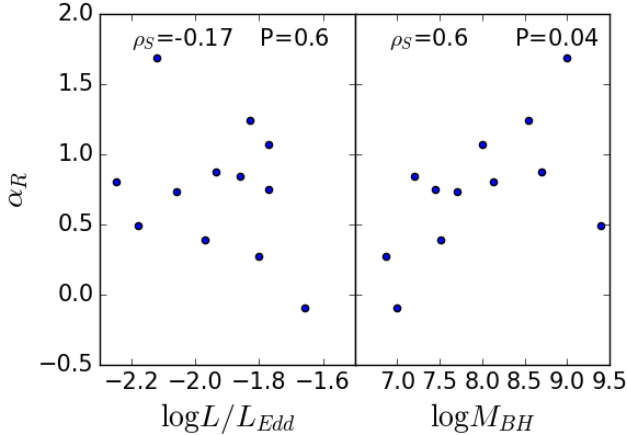
Figure 2. Core spectral index as a function of Eddington ratio (left panel) and BH mass (right panel) in which NGC1275, B3 0309+411B and QSOB0241+62 have not been considered. The results of a Spearman's correlation coefficient analysis are reported in the top.

biguous association of the core, with the effect of a possible dilution of the correlations of the spectral index with either BH mass or Eddington ratio.

5   CLUES ON THE ORIGIN OF RADIO EMISSION

We presented observations for 16 sources. For 2 of them, namely IGRJ00333+6122 and IGRJ16426+6536, the first radio maps ever have been presented in this work, while for other 3 (NGC1142, LEDA168563 and 4U0517+17), we show the first high-frequency (i.e. 22 and 45 GHz) radio maps.

Our JVLA-C observations, with their ~1 arcsec resolution, allow us to sample the sub-kpc scales for our sources. Indeed, considering only the detected sources, with the exception of B30309+411B and IGRJ00333+6122 (at z~0.136 and 0.105, respectively), our observations sample spatial scales from few hundreds of pc to tens of pc, and at these scales.

Our sources show a variety of morphologies, with 8 out of 15 being core dominated, the others being either elongated or exhibiting multiple emitting components. The morphology and the spectral index information we obtained at 22 and 45 GHz allow us to try to discriminate between the possible physical mechanisms which may be at work in AGN at these spatial scales, following the flow-chart suggested by Panessa et al. (2019) (see their Fig. 8). In this scheme, if the emission is resolved on arcseconds scales, then a steep spectral index may suggest either star-formation, if the morphology is clumpy and diffuse, or an outflow (or ionisation cone), if symmetric, otherwise a flat component may suggest a free-free emission. However, a compact, flat-spectrum component, unresolved on arcseconds scale, may suggest emission either from the base of a jet or a corona, therefore tracing the position of the core. In this case high-resolution (mas-scale) observations are required.

In this picture, we can also consider the additional information about the concentration index f_C of the core com-

ponent[10]. The concentration index of the core is a useful tool to quantify the fraction of flux density contained in the compact core. In the case in which in the compact component, identified with the core, additional unresolved components contribute to the emission, then we expect a concentration index <1, as the contribution of these components becomes more and more important; in the case in which the emission of the compact component is actually dominant, a concentration index ~1 is expected.

In the case of the asymmetric double NGC 4388, the flat-spectrum component (NE) could be associated with the core, with a concentration index $f_C \geq 0.75$, while the steeper SW component which could be associated to a jet component. Similar conclusions can be drawn for the other asymmetric double, Mkn 3, in which the core component, having a steeper spectrum, may hide additional (steep) unresolved components ($f_C \sim 0.6$). NGC 1068 exhibits a bipolar outflowing structure, with both compact and extended emission, and the interpretation of the spectral indices in this case is not straightforward. Nevertheless, the extended (~1.2 kpc) structure could be interpreted as the interaction of a radio jet emanating from the nucleus with high-ionisation gas clouds, as also suggested in previous works (e.g. Capetti et al. 1997). NGC 1142, part of the interacting system Arp 118, has a complex morphology, with multiple emitting components distributed on scales of ~19 arcsec in K band, corresponding to ~11 kpc. Component B, identified by the core and having a high (≥0.9) concentration index, is in the centre of a ring-like region, with a southern filament of radio emission and several components at the NE and SW (although only components labelled A1 and A2 are visible at both frequencies). The steep spectrum of the off-nuclear sources, and the complex morphology, suggests a star formation origin of the extended emission, probably produced by the tidal interaction the system is undergoing.

Considering the remaining sources, three of them exhibit an elongated morphology. The maps of NGC 4151 reveal an elongated morphology in the NE-SW direction, with a steep spectrum, compatible with what found at lower frequencies at similar resolution (e.g. Pedlar et al. 1993). This evidence, together with a concentration index of ~ 0.7, could be interpreted as symptom of a non-negligible contribution from optically-thin steep components, from a jet or an outflow (indeed eMERLIN observations at lower frequencies points toward a jet origin, see Williams et al. 2017). Same conclusions can be drawn for MCG +08-11-11 and Mkn 6, with the elongations due to a low power jet or an outflow.

Finally, 8 out 15 sources are characterised by compact morphologies (either unresolved or resolved). Two sources, IGR J00333+6122, and LEDA 168563, exhibit steep spectra, but while for the latter the emission mapped by our observations is on scales of order of ~600 pc, in the former they map scales of ~2.5 kpc. In both cases the emission may be due outflowing optically-thin components, with a contribution from unresolved sub-kpc star formation. In the case of IGR J00333+6122, these steep spectrum components may

---

[10] The concentration index of the core component has been calculated as $f_C = S_{peak}/S_{Int}$, where S_{peak} is the peak intensity and S_{int} is the integrated flux density. For a similar definition see Laor et al. (2019).

be on larger scales, i.e. 1-2 kpc, and therefore we can not exclude a contribution from circumnuclear star formation on these scales. For this source, high resolution observations are required to break this degeneracy and disentangle the contribution of different mechanisms, and for this purpose we will benefit of our VLBI observations, although at lower frequencies. NGC 5252 has two components, the southern one having a steep spectrum, the northern one is detected only in K-band (the association of the northern component with the nucleus, the southern component, has been questioned, see Kim et al. 2015; Yang et al. 2017). One source, NGC 788, exhibit a spectrum which is borderline, i.e. compatible between steep and flat, therefore the interpretation is not straightforward. Higher resolution observations are necessary to draw robust conclusions on the nature of radio emission in these sources.

We note that a possible contribution to the spectral index of steep spectrum components may come from spectral ageing, as higher energy electrons radiates away their energy first, resulting in a steeping of the slope at high frequencies. However, in order to quantify its contribution, high resolution and high sensitivity observations are required over a wide range of frequencies, at a matched resolution, able to resolve possible sub-kpc structures even for compact sources, and to determine the high-frequency spectral break for various regions of the source, having different electron ages. Although we can not rule out a contribution from spectral ageing for steep spectrum sources (both resolved and unresolved ones), since our purpose is to use the spectral index as a tool to discriminate between core components and extended, steep spectrum ones, and establish the dominant radiative mechanisms, it does not affect our main considerations.

Four sources show a flat (QSO B0241+62 and NGC 1275) and inverted (4U 0517+17) spectra and are compact, core-dominated, with B3 0309+411B having a spectrum compatible with both flat and inverted (however for the last source our observations map spatial scales of ~2 kpc). These sources, except for 4U 0517+17, are known powerful radio sources. In these sources, high resolution (i.e. VLBI) monitorings have revealed pc-scale relativistic jets closely aligned to the line-of-sight (MOJAVE Project[11], Lister et al. 2019). This suggests that the evidence of a compact morphology, a flat spectrum and a enhanced radio flux, due to Doppler boosting, can be interpreted as due to a jet closely aligned with the line-of-sight. Although the observations for B3 0309+411B maps larger spatial scales with respect to the other two sources, the same argument can be applied as well. The source 4U 0517+17 is characterised by a flat spectrum, which can be interpreted as signature of either synchrotron emission from the optically-thick base of a jet or emission from a corona. However, higher resolution observations are required to draw more robust conclusions.

A supplementary appendix with notes on individual sources will be available in the online version of the paper.

6 THE X-RAY AND RADIO CORRELATION

Our high frequency observations allow us to investigate also the existence of a correlation between radio luminosity, at either 22 or 45 GHz, and the X-rays one (i.e. 2–10 keV), focusing on the core contribution, as emission from more extended components is expected to fade. Some sources exhibit extended components which may not be AGN related, and some others, despite being compact, may hide extended sources (as suggested by the concentration index), and for this reason we considered the core peak luminosities only. Such correlations have been found (mostly at lower frequencies) for LLAGN and low-hard state XRB, which have been interpreted as symptom of inefficient accretion regime (e.g. Panessa & Giroletti 2013), as well as highly-accreting AGN and 'outliers' XRB, interpreted as symptom of radiatively efficient accretion flows (e.g. Coriat et al. 2011; Dong et al. 2014), in a broad picture of common accretion-ejection physics across different BH masses. Excluding the three known powerful sources, we find a correlation of the form $\log L_R^{peak}(erg\, s^{-1}) \propto m \log L_{2-10\,keV}(erg\, s^{-1})$, with $m =$ 0.66±0.26 and 0.56±0.25 at 22 and 45 GHz, respectively. However, in both cases the statistical significance is low, as a Spearman correlation test results in ρ ~0.6 with P~0.06 at 22 GHz and ρ ~0.5 with P~0.1 at 45 GHz. No definite conclusion can be drawn from this correlation as more sources are required to strengthen this finding. Indeed, so far the relation has been established at lower frequencies and on different scales (e.g. Panessa et al. 2015), where different processes and emitting regions may be involved.

Finally, we tested whether our sources follow the $L_R/L_X \sim 10^{-5}$ relation predicted by coronal models, according to which both radio and X-rays would originate in a magnetically heated corona, the contribution of which should emerge in the (sub)-mm range (e.g. Laor & Behar 2008; Raginski & Laor 2016). As can be seen from Fig. 3, three powerful radio sources tend to depart significantly from the relation, with the rest of the sources roughly following the relation. This result may be interpreted as an indication of a contribution of a magnetically heated corona to the radio emission at these frequencies. A more robust statistical result will be provided by the new data that will be available on this sample.

7 DISCUSSION

The novelty of our strategy with respect to previous works is the use of dual frequency (22 and 45 GHz) observations, which allow us to compute high-frequency spectral indices, couple them with morphological information and eventually discriminate between possible radiative mechanisms regulating radio emission at the sub-kpc scales, except for two sources, B30309+411B and IGRJ00333+6122, for which our observations map scales of order of ~2 kpc (for the former high resolution observations have been already carried out, for the latter we will benefit of our VLBI observations for the sub-kpc scale characterisation).

We note that high-frequency radio observations are particularly useful to target the nuclear emission, as at these frequencies (at our resolutions), the contribution of more extended, optically-thin, steep-spectrum components, which
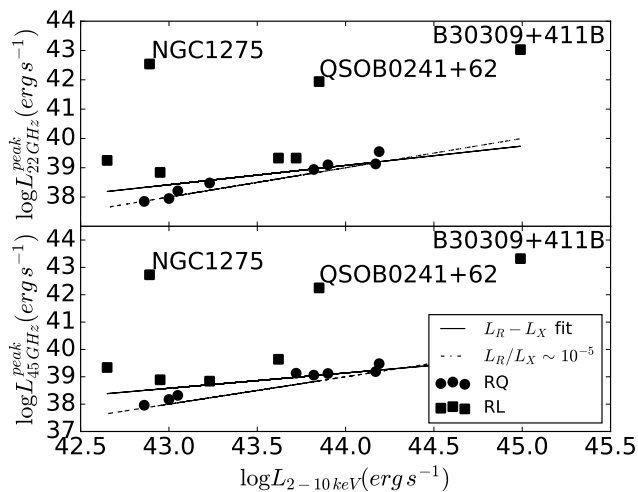
Figure 3. The 22 GHz peak luminosity (top panel) and the 45 GHz peak luminosity (bottom panel) of the core components as a function of the 2-10 keV luminosity. Black squares and black circles represents RL and RQ, respectively, considering the Terashima & Wilson (2003) with $R_X = L_{22\,GHz}/L_{2-10\,keV}$ (top panel) and $R_X = L_{45\,GHz}/L_{2-10\,keV}$ (bottom panel). The black line is a linear fit performed not considering the three radio galaxies B3 0309+411B, NGC1275 and QSOB0241+62, while the black dah-dotted line is the $L_R/L_X \sim 10^{-5}$ line.

may be not AGN-related, is expected to be less and less important, and absorption mechanisms like synchrotron self absorption and free-free absorption are less effective with respect to lower frequencies (e.g. Kellermann 1966; Park et al. 2013).

Moreover, the hard - X-rays selection of the sample makes it ideal for an unbiased characterisation of the radio population at these redshifts, which can be noted considering the distribution of flux densities in Table A1. Our radio characterisation fills a gap in the existing literature. Indeed, our sources are characterised by Eddington ratios at intermediate values between that of LLAGN, usually exhibiting $L_{Bol}/L_{Edd} \leq 10^{-3}$, and the PG quasars, usually only type-1 objects characterised by $L_{Bol}/L_{Edd} \sim 0.1 - 1$, in an intermediate redshift range which partially overlaps with both cases. This gives us the chance to sample the radio emission in an intermediate accretion regime, and test the occurrence of compact vs extended, jet/outflows-like features.

Few works have been devoted to the characterisation of the high frequency emission in a general population of AGN, one of them being that of Park et al. (2013), who characterised the high-frequency (22 and 43 GHz) emission of sample of AGN with single dish measurements. Despite the comparable redshift range and the similar radio luminosities of the detected sources, they find a prevalence of flat/inverted spectra and significantly lower detection rates (37 and 22 per cent at 22 and 43 GHz, respectively). We attribute these differences to a combination of both the different criteria for the selection of the samples and to the single-dish observations. Indeed, the cross match of SDSS-DR7 and FIRST may have led, from a radio point of view, to the selection of powerful objects (because of FIRST sensitivity) with bright extended features which may be not AGN related (because of 5 arcsec FIRST resolution), while

single-dish observations may have encompassed radio emission from the AGN core as well as from extended features.

More recently, Smith et al. (2016, 2020) characterised a sample of hard-X-rays selected AGN from Swift-BAT at 22 GHz at ~1 arcsec resolution, with most of properties similar to our sample, e.g. redshift range, sensitivity of the hard-X-rays instrument, X-ray and hard-X-rays luminosities, and sensitivity of radio observations. The high detection rate found for our observations (15 out of 16 sources) is in agreement with what found by Smith et al., and a similar conclusion can be drawn considering the morphologies of the sources, as they find that more than half of the sources have a compact morphology. However, they also find that a high fraction (30/96 sources) has a morphology compatible with star formation, with only 11 sources compatible with hosting sub-kpc to kpc scale jets. The interpretation of our high-frequency spectral indices and morphologies led us to different conclusions, according to which for only one source, namely NGC1142, the kpc-scale radio emission is star formation related (as a result of tidal interaction in an interacting system), while for other 6 sources it is compatible with presence of a jet. However, this does not exclude the contribution of star formation. Indeed, while our high-frequency, ~1 arcsec resolution observations are effective in isolating the core AGN emission with respect to the extended one, which may be not AGN-related, a contribution from sub-kpc, nuclear star formation may be present as well (e.g. Smith et al. 2016, 2020).

We have also found, in agreement with Smith et al. (2016, 2020), that our sources, with the exception of three powerful sources (see Fig. 3), roughly follow the Güdel-Benz relation $L_R/L_X \sim 10^{-5}$ valid for coronally active stars (Guedel & Benz 1993), which have been interpreted in the sense of a common origin in a magnetically-heated corona of both radio and X-rays emission (e.g. Laor & Behar 2008). However, it is not straightforward to disentangle the contribution of a corona from that of a low-power, sub-kpc scale radio jet. Recently, Baek et al. (2019) have performed a VLBI characterisation at 22 GHz for a number of radio bright hard-X-rays selected AGN from the Swift-BAT sample, proving that pc-scale jets in these sources are not common. However, this may not be the case for the fainter hard-X-ray selected AGN (as some members of our sample), in which less powerful, less collimated jets may be present. In our discussion about the origin of the radio emission in our sources we referred to the flow chart in Panessa et al. (2019) (their Figure 8). In less powerful, compact sources, in order to disentangle the contribution of a corona to that of a sub-kpc scale low-power jet, multi-frequency high-resolution observations are required, but the definite proof would be a monitoring of the correlated radio and X-ray variability following the Neupert effect, predicted in coronal models. This promising methodology is only at an early stage (e.g. in Behar et al. 2020, for NGC7469).

Finally, we note that, although only a part of our sample of 44 sources have been observed (16/44 sources), we expect the properties we have found in this work to be representative of that of the full sample. Indeed, as explained before, the observations of our sources have been carried out in a random way, i.e. without introducing any selection bias, as can be appreciated in histograms in Fig. 1. We ex-

pect that the future JVLA observations in our program will likely strengthen our findings statistically.

8 CONCLUSIONS

In this work we presented the results of a high-frequency (22 and 45 GHz) JVLA observational campaign for a sample of relatively nearby (0.0033≤z≤0.323) hard - X-rays selected AGN. The resolution the JVLA C-configuration guarantees us (≤1 arcsec) allow us to probe linear scales of ∼70 pc for the nearest one (NGC 4151) and ∼2.4 kpc for the farthest one (B3 0309+411B).

We can summarise our main results as following:

- Our strategy translates into high detection rates at both frequencies, i.e. 15 out of 16, 89±16 per cent. The only undetected source, namely IGRJ 16426+6536, is a NLS1, for which we derive 3-sigma upper limits at 24 and 162 μJy beam^{-1} level at K and Q bands, respectively.

- The flux densities range from hundreds of μJy up to hundreds of mJy (radio luminosities in the range $37 \leq log \nu L_\nu (ergs^{-1}) \leq 40$). Three sources, which are known powerful radio sources, have significantly higher flux densities (up to tens of Jy).

- We find a compact core in all of the detected sources, of which 8/15 are core-dominated, while 7/15 exhibit extended structures (e.g. double, elongated and multiple components). The spectral indices of the components range from steep to flat/inverted, suggesting that the expected compact, flat-spectrum core may not be dominant and emission from optically-thin, steep spectrum components may be not negligible.

- Different physical mechanisms may be responsible for the radio emission, a core + low power jet or an outflow, the base of a jet or a corona , star formation from tidal interaction, or a jet closely aligned to the line-of-sight. For four sources, the interpretation is not straightforward.

- In the case of our sample the radio/X-ray radio-loudness parameter does not separate univocally the RL AGN, which are expected to be powered by relativistic jets, and the RQ AGN where different astrophysical procesess compete (weak jet, SF, disc wind, outflowing magnetically-active corona). We conclude that such a parameter cannot be used to distiguish between the properties of two populations. The three sources well known to be strong radio sources indeed differ significantly from the rest of the sample.

- We found indication of a correlation between the 22 and 45 GHz core luminosities and the 2-10 keV luminosity, with slopes of 0.66±0.26 and 0.56±0.25, respectively, suggesting a connection between the accretion and ejection processes holding at relatively higher frequencies. The statistical significance of the relations is low, therefore larger samples are required to derive more robust results.

- The sources roughly follow the $L_R/L_X \sim 10^{-5}$ relation proposed by coronal models (e.g. Laor & Behar 2008), suggesting a contribution to the radio emission from a hot corona, with the three powerful radio sources which seems to depart significantly from the relation, as expected.

Our results suggest that even at high-frequencies the compact, flat-spectrum core is present, but it is not always dominant, as originally expected, and that steep-spectrum components on scales mapped by our observations (smaller than ∼ kpc) can contribute in a non negligible way.

The high-frequency band in the radio represents a unique tool to study the emission mechanisms of this population of AGN, as it allows to target their nuclear component, thanks to the increasing resolution with frequency, being relatively safe from absorption mechanisms with respect to lower frequencies. A more thorough characterisation at these frequencies will be possible with unprecedented resolution and sensitivity of the next generation interferometers. Indeed, the Square Kilometre Array (SKA) in its phase 1 (SKA1) will extend up to 15 GHz, while in its phase 2 (SKA2) it is expected to extend up to 30 GHz (e.g. Braun et al. 2019), while the next-generation VLA (ngVLA) will cover frequencies up to 116 GHz (Selina et al. 2018).

REFERENCES

Ayani K., Iye M., 1989, AJ, 97, 686
Baek J., et al., 2019, MNRAS, 488, 4317
Baldi R. D., Behar E., Laor A., Horesh A., 2015, MNRAS, 454, 4277
Baldi R. D., et al., 2018, MNRAS, 476, 3478
Barvainis R., Lonsdale C., Antonucci R., 1996, AJ, 111, 1431
Begelman M. C., Armitage P. J., 2014, ApJ, 782, L18
Begelman M. C., Blandford R. D., Rees M. J., 1984, Reviews of Modern Physics, 56, 255
Behar E., Baldi R. D., Laor A., Horesh A., Stevens J., Tzioumis T., 2015, MNRAS, 451, 517
Behar E., Vogel S., Baldi R. D., Smith K. L., Mushotzky R. F., 2018, MNRAS, 478, 399
Behar E., et al., 2020, MNRAS, 491, 3523
Bird A. J., et al., 2007, ApJS, 170, 175
Blustin A. J., Fabian A. C., 2009, MNRAS, 396, 1732
Bock D. C. J., Large M. I., Sadler E. M., 1999, AJ, 117, 1578
Booler R. V., Pedlar A., Davies R. D., 1982, MNRAS, 199, 229
Braun R., Bonaldi A., Bourke T., Keane E., Wagg J., 2019, arXiv e-prints, p. arXiv:1912.12699
Briggs D. S., 1995, in American Astronomical Society Meeting Abstracts. p. 1444
Brinkmann W., Laurent-Muehleisen S. A., Voges W., Siebert J., Becker R. H., Brotherton M. S., White R. L., Gregg M. D., 2000, A&A, 356, 445
Bruni G., et al., 2019, ApJ, 875, 88

Table 3. The derived quantities for the 15 detected objects in the sample. The radio luminosities are that of the core components, when it has been possible to identify them, as well as the radio-loudness parameters R_X, and the peak flux density has been considered. Same argument applies for the spectral index. The 2-10 keV absorption-corrected luminosities are from Panessa et al. (2015), unless otherwise specified.

Target	$L_{22\,GHz}$ (erg s^{-1})	$L_{45\,GHz}$ (erg s^{-1})	$L_{2-10\,keV}$ (erg s^{-1})	α	M_{BH} ($M_\odot$)	L/L_{Edd}	f_C(K)	f_C(Q)	f_C(Q$_t$)	R_X(22\,GHz)	R_X(45\,GHz)	R_O	Ref
(1)	(2)	(3)	(4)	(5)	(6)	(7)	(8)	(9)	(10)	(11)	(12)	(13)	(14)
IGRJ00333+6122	39.55	39.48	44.19	+1.24	8.54	-1.83	0.89	0.58	0.87	-4.64	-4.71	1.9	Masetti et al. (2009)
NGC788	37.85	37.96	42.86	+0.39	7.51	-1.97	0.92	0.89	0.75	-5.01	-4.9	-0.93	Woo & Urry (2002)
NGC1068	38.838	38.89	42.95	+0.84	7.2	-1.86	0.77	0.57	0.76	-4.11	-4.06	2.11	Greenhill et al. (1996)
QSOB0241+62	41.94	42.25	43.85*	+0.35	8.09	-1.809	0.99	0.99	0.99	-1.91	-1.6	1.15	Koss et al. (2017)
NGC1142	38.94	39.06	43.82	+0.49	9.4	-2.18	0.94	0.99	0.86	-4.88	-4.76	0.15	Winter et al. (2009)
B3 0309+411B	43.025	43.320	44.99	+0.06	-	-	0.99	0.99	0.99	-1.96	-1.67	3.2	
NGC1275	42.54	42.73	42.89	+0.4	8.5	-2.18	0.99	0.99	0.99	-0.35	-0.16	2.99	Woo & Urry (2002)
LEDA168563	39.1	39.12	43.90	+1.07	8.0	-1.77	0.94	0.93	0.99	-4.8	-4.8	1.51	Vasudevan et al. (2009)
4U0517+17	38.48	38.84	43.23	-0.097	7.0	-1.658	0.92	0.95	0.98	-4.75	-4.39	0	Stalin et al. (2011)
MCG+08-11-11	39.33	39.64	43.62*	+0.75	7.45	-1.77	0.65	0.57	0.76	-4.29	-3.98	1.23	Fausnaugh et al. (2017)
Mkn3	39.13	39.19	44.17	+0.87	8.7	-1.936	0.60	0.47	0.61	-5.04	-4.98	0.95	Woo & Urry (2002)
Mkn6	39.25	39.34	42.65*	+0.8	8.13	-2.25	0.62	0.74	0.64	-3.4	-3.31	1.38	Grier et al. (2012)
NGC4151	38.21	38.32	43.05	+0.73	7.7	-2.06	0.71	0.71	0.74	-4.84	-4.73	0.61	Greene et al. (2016)
NGC4388	37.95	38.17	43.00	+0.27	6.86	-1.803	0.75	0.83	0.74	-5.05	-4.83	-1.01	Greene et al. (2016)
NGC5252	39.33	39.13	43.72	+1.68	9.0	-2.12	0.93	0.94	0.91	-4.39	-4.59	0.68	Graham (2008)

Column (1), name of the source; Column (2), 22 GHz peak luminosity; Columns (3), 45 GHz peak luminosity; Column (4), 2-10 keV luminosity; Column (5), core spectral index; Column (6), black hole mass; Column (7), Eddington ratio; Column (8), concentration index in K band; Column (9), concentration index in Q band; Column (10), concentration index in tapered Q band; Column(11), $R_X(22\,GHz) = \log L_{22\,GHz} - \log L_{2-10\,keV}$; Column (12), $R_X(45\,GHz) = \log L_{45\,GHz} - \log L_{2-10\,keV}$; Column (13), $R_O = \log S_{5\,GHz} - \log S_B$; Column (14), reference for M_{BH}.
* X-rays luminosity from Molina et al. (2019).

Burlon D., Ghirlanda G., Murphy T., Chhetri R., Sadler E., Ajello M., 2013, MNRAS, 431, 2471

Buttiglione S., Capetti A., Celotti A., Axon D. J., Chiaberge M., Macchetto F. D., Sparks W. B., 2010, A&A, 509, A6

Capetti A., Macchetto F. D., Lattanzi M. G., 1997, ApJ, 476, L67

Carral P., Turner J. L., Ho P. T. P., 1990, ApJ, 362, 434

Charlot P., et al., 2010, AJ, 139, 1713

Chiaraluce E., Bruni G., Panessa F., Giroletti M., Orienti M., Rampadarath H., Vagnetti F., Tombesi F., 2019, MNRAS, 485, 3185

Condon J. J., Helou G., Sanders D. B., Soifer B. T., 1990, ApJS, 73, 359

Condon J. J., Cotton W. D., Greisen E. W., Yin Q. F., Perley R. A., Taylor G. B., Broderick J. J., 1998, AJ, 115, 1693

Coriat M., et al., 2011, MNRAS, 414, 677

Cotton W. D., Jaffe W., Perrin G., Woillez J., 2008, A&A, 477, 517

Crenshaw D. M., Kraemer S. B., Hutchings J. B., Danks A. C., Gull T. R., Kaiser M. E., Nelson C. H., Weistrop D., 2000, ApJ, 545, L27

Damas-Segovia A., et al., 2016, ApJ, 824, 30

Doi A., Inoue Y., 2016, PASJ, 68, 56

Doi A., Nakanishi K., Nagai H., Kohno K., Kameno S., 2011, AJ, 142, 167

Dong A.-J., Wu Q., Cao X.-F., 2014, ApJ, 787, L20

Falcke H., Biermann P. L., 1995, A&A, 293, 665

Falcke H., Wilson A. S., Simpson C., 1998, ApJ, 502, 199

Falcke H., Körding E., Markoff S., 2004, A&A, 414, 895

Fausnaugh M. M., et al., 2017, ApJ, 840, 97

Fender R., Belloni T., 2012, Science, 337, 540

Ferrarese L., Ford H., 2005, Space Sci. Rev., 116, 523

Ferrarese L., Merritt D., 2000, ApJ, 539, L9

Gallimore J. F., Baum S. A., O'Dea C. P., Pedlar A., 1996a, ApJ, 458, 136

Gallimore J. F., Baum S. A., O'Dea C. P., 1996b, ApJ, 464, 198

Gallimore J. F., Baum S. A., O'Dea C. P., 2004, ApJ, 613, 794

Giovannini G., et al., 2018, Nature Astronomy, 2, 472

Giroletti M., Panessa F., 2009, ApJ, 706, L260

Graham A. W., 2008, ApJ, 680, 143

Greene J. E., et al., 2016, ApJ, 826, L32

Greenhill L. J., Gwinn C. R., Antonucci R., Barvainis R., 1996, ApJ, 472, L21

Grier C. J., et al., 2012, ApJ, 755, 60

Guedel M., Benz A. O., 1993, ApJ, 405, L63

Healey S. E., Romani R. W., Taylor G. B., Sadler E. M., Ricci R., Murphy T., Ulvestad J. S., Winn J. N., 2007, ApJS, 171, 61

Heckman T. M., Best P. N., 2014, ARA&A, 52, 589

Hervet O., Boisson C., Sol H., 2016, A&A, 592, A22

Ho L. C., Ulvestad J. S., 2001, ApJS, 133, 77

Högbom J. A., 1974, A&AS, 15, 417

Hummel E., Saikia D. J., 1991, A&A, 249, 43

Jarosik N., et al., 2011, ApJS, 192, 14

Johnston K. J., Elvis M., Kjer D., Shen B. S. P., 1982, ApJ, 262, 61

Joy M., Ghigo F. D., 1988, ApJ, 332, 179

Kellermann K. I., 1966, ApJ, 146, 621

Kellermann K. I., Sramek R., Schmidt M., Shaffer D. B., Green R., 1989, AJ, 98, 1195

Kellermann K. I., Sramek R. A., Schmidt M., Green R. F., Shaffer D. B., 1994, AJ, 108, 1163

Kharb P., O'Dea C. P., Baum S. A., Colbert E. J. M., Xu C., 2006, ApJ, 652, 177

Kharb P., O'Dea C. P., Baum S. A., Hardcastle M. J., Dicken D., Croston J. H., Mingo B., Noel-Storr J., 2014, MNRAS, 440, 2976

Kim M., et al., 2015, ApJ, 814, 8

Konar C., Saikia D. J., Ishwara-Chandra C. H., Kulkarni V. K., 2004, MNRAS, 355, 845

Koss M., et al., 2017, ApJ, 850, 74

Kukula M. J., Ghosh T., Pedlar A., Schilizzi R. T., Miley G. K., de Bruyn A. G., 1993, MNRAS, 264, 893

Kukula M. J., Pedlar A., Baum S. A., O'Dea C. P., 1995a, MNRAS, 276, 1262

Kukula M. J., Pedlar A., Baum S. A., O'Dea C. P., 1995b, MNRAS, 276, 1262

Kukula M. J., Dunlop J. S., Hughes D. H., Rawlings S., 1998, MNRAS, 297, 366

Kukula M. J., Ghosh T., Pedlar A., Schilizzi R. T., 1999, ApJ, 518, 117

Laor A., Behar E., 2008, MNRAS, 390, 847

Laor A., Baldi R. D., Behar E., 2019, MNRAS, 482, 5513

Leipski C., Falcke H., Bennert N., Hüttemeister S., 2006, A&A, 455, 161

Lister M. L., Gower A. C., Hutchings J. B., 1994, AJ, 108, 821

Lister M. L., Aller M. F., Aller H. D., Hodge M. A., Homan D. C., Kovalev Y. Y., Pushkarev A. B., Savolainen T., 2018, ApJS, 234, 12

Lister M. L., et al., 2019, ApJ, 874, 43

Lusso E., et al., 2012, MNRAS, 425, 623

Maccarone T. J., 2003, A&A, 409, 697

Magorrian J., et al., 1998, AJ, 115, 2285

Malizia A., Stephen J. B., Bassani L., Bird A. J., Panessa F., Ubertini P., 2009, MNRAS, 399, 944

Malizia A., Molina M., Bassani L., Stephen J. B., Bazzano A., Ubertini P., Bird A. J., 2014, ApJ, 782, L25

Masetti N., et al., 2009, A&A, 495, 121

Masetti N., et al., 2012, A&A, 538, A123

Mauch T., Murphy T., Buttery H. J., Curran J., Hunstead R. W., Piestrzynski B., Robertson J. G., Sadler E. M., 2003, MNRAS, 342, 1117

McLure R. J., Jarvis M. J., 2002, MNRAS, 337, 109

McMullin J. P., Waters B., Schiebel D., Young W., Golap K., 2007, in Shaw R. A., Hill F., Bell D. J., eds, Astronomical Society of the Pacific Conference Series Vol. 376, Astronomical Data Analysis Software and Systems XVI. p. 127

Merloni A., Heinz S., di Matteo T., 2003, MNRAS, 345, 1057

Middelberg E., et al., 2004, A&A, 417, 925

Molina M., Bassani L., Malizia A., Stephen J. B., Bird A. J., Bazzano A., Ubertini P., 2013, MNRAS, 433, 1687

Molina M., Malizia A., Bassani L., Ursini F., Bazzano A., Ubertini P., 2019, MNRAS, 484, 2735

Mundell C. G., Wilson A. S., Ulvestad J. S., Roy A. L., 2000, ApJ, 529, 816

Mundell C. G., Wrobel J. M., Pedlar A., Gallimore J. F., 2003, ApJ, 583, 192

Nagai H., et al., 2010, PASJ, 62, L11

Nagar N. M., Wilson A. S., Mulchaey J. S., Gallimore J. F., 1999, ApJS, 120, 209

Nagar N. M., Falcke H., Wilson A. S., Ulvestad J. S., 2002, A&A, 392, 53

Narayan R., Yi I., 1994, ApJ, 428, L13

Nims J., Quataert E., Faucher-Giguère C.-A., 2015, MNRAS, 447, 3612

Orienti M., Prieto M. A., 2010, MNRAS, 401, 2599

Padovani P., 2016, A&ARv, 24, 13

Panessa F., Giroletti M., 2013, MNRAS, 432, 1138

Panessa F., Barcons X., Bassani L., Cappi M., Carrera F. J., Ho L. C., Pellegrini S., 2007, A&A, 467, 519

Panessa F., et al., 2011, MNRAS, 417, 2426

Panessa F., et al., 2015, MNRAS, 447, 1289

Panessa F., et al., 2016, MNRAS, 461, 3153

Panessa F., Baldi R. D., Laor A., Padovani P., Behar E., McHardy I., 2019, arXiv e-prints,

Park S., Sohn B. W., Yi S. K., 2013, A&A, 560, A80

Patnaik A. R., Browne I. W. A., Wilkinson P. N., Wrobel J. M., 1992, MNRAS, 254, 655

Pedlar A., Booler R. V., Spencer R. E., Stewart O. J., 1983, MNRAS, 202, 647

Pedlar A., Ghataure H. S., Davies R. D., Harrison B. A., Perley R., Crane P. C., Unger S. W., 1990, MNRAS, 246, 477

Pedlar A., Kukula M. J., Longley D. P. T., Muxlow T. W. B., Axon D. J., Baum S., O'Dea C., Unger S. W., 1993, MNRAS, 263, 471

Perley R. A., Butler B. J., 2017, ApJS, 230, 7

Peterson B. M., 2003, Masses of Supermassive Black Holes in Active Galactic Nuclei. p. 43

Petrucci P.-O., Ferreira J., Henri G., Pelletier G., 2008, MNRAS, 385, L88

Preston R. A., Morabito D. D., Williams J. G., Faulkner J., Jauncey D. L., Nicolson G., 1985, AJ, 90, 1599

Raginski I., Laor A., 2016, MNRAS, 459, 2082

Robitaille T., Bressert E., 2012, APLpy: Astronomical Plotting Library in Python (ascl:1208.017)

Roy A. L., Colbert E. J. M., Wilson A. S., Ulvestad J. S., 1998, ApJ, 504, 147

Saikia D. J., Shastri P., Sinha R. P., Kapahi V. K., Swarup G., 1984, Journal of Astrophysics and Astronomy, 5, 429

Salvato M., Greiner J., Kuhlbrodt B., 2004, ApJ, 600, L31

Sauro J., Lewis J. R., 2005, Proceedings of the Human Factors and Ergonomics Society Annual Meeting, 49, 2100

Schmelz J. T., Feigelson E. D., Schwartz D. A., 1986, AJ, 92, 585

Schmitt H. R., Ulvestad J. S., Antonucci R. R. J., Kinney A. L., 2001, ApJS, 132, 199

Selina R. J., et al., 2018, The ngVLA Reference Design. p. 15

Smith K. L., Mushotzky R. F., Vogel S., Shimizu T. T., Miller N., 2016, ApJ, 832, 163

Smith K. L., et al., 2020, MNRAS, p. 3237

Stalin C. S., Jeyakumar S., Coziol R., Pawase R. S., Thakur S. S., 2011, MNRAS, 416, 225

Suzuki K., et al., 2012, ApJ, 746, 140

Tadhunter C., Tsvetanov Z., 1989, Nature, 341, 422

Taylor G. B., Vermeulen R. C., Readhead A. C. S., Pearson T. J., Henstock D. R., Wilkinson P. N., 1996a, ApJS, 107, 37

Taylor G. B., Vermeulen R. C., Readhead A. C. S., Pearson T. J., Henstock D. R., Wilkinson P. N., 1996b, ApJS, 107, 37

Terashima Y., Wilson A. S., 2003, ApJ, 583, 145

Thean A., Pedlar A., Kukula M. J., Baum S. A., O'Dea C. P., 2000, MNRAS, 314, 573

Thean A. H. C., Gillibrand T. I., Pedlar A., Kukula M. J., 2001, MNRAS, 327, 369

Tsvetanov Z. I., Morse J. A., Wilson A. S., Cecil G., 1996, ApJ, 458, 172

Ulvestad J. S., Wilson A. S., 1986, MNRAS, 218, 711

Ulvestad J. S., Wilson A. S., 1989, ApJ, 343, 659

Ulvestad J. S., Wilson A. S., Sramek R. A., 1981, ApJ, 247, 419

Ulvestad J. S., Neff S. G., Wilson A. S., 1987, AJ, 93, 22

Ulvestad J. S., Wong D. S., Taylor G. B., Gallimore J. F., Mundell C. G., 2005, AJ, 130, 936

Vasudevan R. V., Mushotzky R. F., Winter L. M., Fabian A. C., 2009, MNRAS, 399, 1553

Walker R. C., Dhawan V., Romney J. D., Kellermann K. I., Vermeulen R. C., 2000, ApJ, 530, 233

Whittle M., Rosario D. J., Silverman J. D., Nelson C. H., Wilson A. S., 2005, AJ, 129, 104

Williams D. R. A., et al., 2017, MNRAS, 472, 3842

Wilson A. S., 1981, in Battrick B., Mort J., eds, ESA Special Publication Vol. 162, Optical Jets in Galaxies. pp 125–130

Wilson A. S., Tsvetanov Z. I., 1994, AJ, 107, 1227

Wilson A. S., Ulvestad J. S., 1982, ApJ, 263, 576

Wilson A. S., Ulvestad J. S., 1983, ApJ, 275, 8

Wilson A. S., Willis A. G., 1980, ApJ, 240, 429

Wilson A. S., Pooley G. G., Willis A. G., Clements E. D., 1980, ApJ, 237, L61

Winter L. M., Mushotzky R. F., Reynolds C. S., Tueller J., 2009, ApJ, 690, 1322

Woo J.-H., Urry C. M., 2002, ApJ, 579, 530

Yang X., et al., 2017, MNRAS, 464, L70

Yong S. Y., Webster R. L., King A. L., 2016, Publ. Astron. Soc. Australia, 33, e009

Zakamska N. L., et al., 2016, MNRAS, 455, 4191

de Bruyn A. G., 1989, A&A, 226, L13

de Rosa A., et al., 2012, MNRAS, 420, 2087

van der Hulst J. M., Crane P. C., Keel W. C., 1981, AJ, 86, 1175

van der Hulst J. M., Hummel E., Dickey J. M., 1982, ApJ, 261, L59

APPENDIX A: NOTES ON INDIVIDUAL SOURCES AND RADIO MAPS

4U0517+17 This source have been studied by (Schmelz et al. 1986) with the VLA in C configuration. They put an upper limit of ~1.1 mJy for the flux density at 20 cm. Panessa et al. (2015) derive a flux of ~6.1 mJy with NVSS (45 arcsec resolution), finding a slightly resolved morphology. Our data at 22 and 45 GHz reveal compact morphology, either slightly resolved (at 22 GHz) or unresolved (at

45 GHz). Flux densities are of the order of 2 - 2.5 mJy, and the spectral index is flat/inverted α =-0.097±0.11, which can be interpreted as signature of either emission from the optically-thick base of a jet or from a corona.

B3 0309+411B It is a well-known broad line radio galaxy, with Mpc-scale structure, with a milliarcsecond core with a quasar-like spectrum highly varying in the radio de Bruyn (1989). The core is found to have a slightly inverted radio spectrum and it is responsible for nearly 75 per cent of the total emission. A weak extension towards PA~70 deg is reported by Patnaik et al. (1992) with VLA in A configuration at 8.4 GHz. At higher resolutions, VLBI studies revealed a kpc and a pc-scale jet-like feature in the north-west direction (e.g. Taylor et al. 1996a; Lister et al. 2018) with a flat spectral index (see also Konar et al. 2004). Recently, it has been studied by our group (Bruni et al. 2019) finding that the core exhibit an inverted spectrum in the GHz range, which have been interpreted as signature of a possible high-frequency peak, and thus a young age for the radio core, probably restarted. Our observations reveal a compact morphology, either slightly resolved (22 GHz) or unresolved (45 GHz), in agreement with previous studies at similar resolution (Saikia et al. 1984, at 15 GHz with VLA in C-configuration), with flux densities of the order of ~1 mJy. The spectral index is compatible with flat/inverted, in agreement with previous studies. We can interpret this evidence, together with the enhanced radio flux, as due to a jet closely aligned with the line of sight, as suggested by VLBI monitoring of the pc-scale jet in the MOJAVE project (e.g. Lister et al. 2019). However, considering the lower frequencies SED points in Bruni et al. (2019), this evidence could suggest that the turnover of the spectrum is occurring at these frequencies, confirming the high-frequency peaked scenario.

QSOB0241+62 It has been the subject of many VLA and VLBI studies, which revealed a flat-spectrum core plus a jet-like feature in the SE direction lobe morphology (Preston et al. 1985; Lister et al. 1994, 2018), and the morphology is also reported at 22 and 43 GHz (Charlot et al. 2010). In our VLA maps at 22 and 45 GHz we do not observe hint of jet-like structure at either frequencies, although the source is slightly resolved (but still compact) in both cases. The high measured flux densities are in the range 700 - 900 mJy, with a spectral index which is compatible with flat, which can be interpreted in the light of a jet closely aligned with the line-of-sight, (see the MOJAVE project page Lister et al. 2019), in agreement with the Flat-Spectrum Radio Quasar (FSRQ) classification Hervet et al. (2016).

NGC1275 It is a Sy 2 galaxy identified with the well known radio source 3C84, but Buttiglione et al. (2010) re-classify it as a Low Excitation Galaxy (LEG). VLA maps reveal a flat-spectrum core + extended features in the NS direction, the core having flux densities in the range 20.6 - 22 Jy (6 and 20 cm, Ho & Ulvestad 2001). High resolution observations reveal a radio morphology with multiple lobes at different position angles on different scales, from pc to tens kpc scale (e.g. Pedlar et al. 1990; Walker et al. 2000; Giovannini et al. 2018). Monitoring studies of 3C84 have revealed that it is characterised by recurrent jet activity in its central regions (e.g. Lister et al. 2019), confirmed at high frequencies (see Suzuki et al. 2012). Our maps reveal a compact morphology, either slightly resolved (22 GHz) or unresolved (45 GHz),

with flux densities in the range 17.4 - 23 Jy, and a ~ flat spectral index. Our observations can be explained in terms of a jet closely aligned with the line-of-sight.

NGC788 Ulvestad & Wilson (1989) studied it with VLA at 6 and 20 cm (~ 1 arcsec resolution), reporting an unresolved morphology, fluxes of 1-2 mJy and a borderline spectral index between steep and flat (α ~0.47), see also Nagar et al. (1999). With 1" 22 GHz observation, Smith et al. (2020) observe an slightly extended morphology, interpreted as due to star formation, with flux density of ~0.61 mJy. Our ~1 arcsec resolution maps reveal a compact, core-dominated morphology, with a 22 GHz flux density of 0.87±0.06, higher respect to Smith et al. (2020), and a spectral index of α = 0.4±0.2, compatible with that derived by Ulvestad & Wilson at similar resolution.

IGRJ00333+6122 The only existing work comprising this source is the 1.4 GHz NVSS characterisation made by our group in Panessa et al. (2015). The flux density at 1.4 GHz is ~9.5 mJy with a compact, unresolved morphology at the 45 arcsec resolution. Even at the ~1 arcsec resolution level of our map the source remain unresolved, with flux densities smaller that ~690 μJy, with a steep spectral index α ~1.25±0.4 .

LEDA168563 The only existing work is by our group (Panessa et al. 2015), who reported flux density of ~ 15 mJy at 1.4 GHz with NVSS. Our radio maps reveal a compact morphology either slightly resolved (22 GHz) or unresolved (45 GHz), with flux densities in the range 1.5 - 3.2 mJy, and a steep (α ~1.07±0.12) spectral index.

NGC4151 It has been the subject of many studies at different resolution and frequency bands. VLA 5 GHz 1 arcsec maps reveal an elongated structure (P.A. ~84 deg) with a steep (~ 0.83) spectral index (e.g. Ulvestad et al. 1981; Wilson & Ulvestad 1982). Higher resolution observations have resolved the elongated structure into five (Johnston et al. 1982, 0.6" resolution) and 6 components, with one of them (C4 in their nomenclature) which has a flat spectrum and high brightness temperature, likely to be the AGN nucleus (VLA 0.2" resolution at 15 GHz Carral et al. 1990). Combining VLA and MERLIN observations at 5 and 8 GHz Pedlar et al. (1993) find a two-sided jet at PA~ 77 deg, confirming that there is a flat-spectrum component exhibiting a 150-mas scale jet. Mundell et al. (2003) with VLA and VLBA observations further resolve the nucleus in three components, see also Ulvestad et al. (2005). Recently Williams et al. (2017) report a significant variability in the core flux density (factor of 2) in their eMERLIN maps at 1.51 GHz. Our radio maps suggest an elongated morphology of the radio emission at both frequencies at position angles of 75.7±0.3 and 72±1 deg at 22 and 45 GHz, respectively, with a spectral index which is steep (α =0.7±0.1), in agreement with works at similar resolutions (e.g. Booler et al. 1982; Johnston et al. 1982) and with a jet scenario.

NGC5252 It is a Sy1.9 galaxy which is known to exhibit pair of ionisation cones in optical emission lines images (e.g. Tadhunter & Tsvetanov 1989). Previous VLA studies revealed two components ~10 kpc far, one (the southern) coincident with optical nucleus, the other (northern) which can be associated with emission line features, both having steep spectra (e.g. Wilson & Tsvetanov 1994; Tsvetanov et al. 1996; Kukula et al. 1995a). Yang et al. (2017) performed

EVN observations focusing on the off-nuclear component, finding that it is compact on pc scale, it has a flat spectrum and a high brightness temperature ($T_B \geq 10^7$ K), which is interpreted as signature of a background LLAGN. Our radio maps exhibit a compact, resolved core and a northern component ~22 arcsec far (~ 10 kpc) which is however detected only at 22 GHz. The flux densities for the nuclear component are ~8.8 and 2.7 mJy at 22 and 45 GHz, while the 22 GHz flux of the northern component is ~0.6 mJy. The nuclear component has a steep spectrum.

Mkn6 Previous VLA studies reveal that Mkn 6 possesses radio emission on three spatial scales: i) ~1 kpc scale jet NE-SW direction, with two components ~ 1 arcsec apart; ii) bubbles on scales ≥1.5 kpc E-W direction; iii) bubbles on scales ≥4.5 kpc (Kharb et al. 2006). This complex structure may be due to either a jet precession and/or the jet interaction with ambient interstellar medium. Kharb et al. (2014) performed VLBA observations spotting the presence of a core with a high brightness temperature (T_B ~10^8 K), interpreted as the optically-thick base of the jet, the other components of the jets being elongated and having steeper spectra. Our radio maps reveal a resolved morphology elongated in the N-S direction. The double structure seen by e.g. Ulvestad et al. is seen only in the full-resolution Q -band maps, with a separation of ~1 arcsec. Considering the 22 GHz and the naturally-weighted, untapered Q-band maps, the flux densities are of 9.7 and 16.6 mJyand the spectral index is steep, compatible with previous studies at similar resolution (e.g. van der Hulst et al. 1981).

MCG+08-11-11

VLA maps at 8.4 GHz revealed a central component (P.A. ~ 128 deg) and an extended one on scales ~1.2 kpc in the N-S direction (Wilson & Willis 1980; Schmitt et al. 2001) while VLBI observations a 2 and 6 cm resolve the center into three components (0.7" length NW-SE direction, P.A. = 127 deg)with a component having a flatter spectrum (recognized as the core) and a 2.4 kpc emission on N-S direction. Behar et al. (2018) observed it at 100 GHz with CARMA finding a flux density of 7.53±0.19 and a spectral slope, calculated within the CARMA 100 GHz band, of 0.47±0.29. Smith et al. (2020) 1" resolution 22 GHz map reveal a morphology compatible with ours, with a flux density 0f ~13.8 mJy smaller than our 15.6±0.8mJy. Our radio maps exhibit a en elongated structure in the N-S direction with P.A. = 160±1 and 131±16 deg at 22 and 45 GHz, respectively. The flux densities for the compact component are of order of 15.7 - 9.3 mJy, with a spectral index of 0.75±0.11. The above results are compatible with previous VLA works at similar resolutions (e.g. Wilson & Willis 1980; Ulvestad & Wilson 1986).

Mkn3 Previous VLA maps reveal an asymmetric double morphology extending for ~600 pc in the E-W direction, with the two components having steep spectra (e.g. Wilson et al. 1980). High resolutions observations resolve it into eight components in an S-shaped structure, with the closest component to the optical position having flat spectrum and recognized as the nucleus (e.g. Kukula et al. 1993, 1999). Our radio maps reveal a double morphology in the E-W direction, with components which are 1.5 arcsec apart (~400 pc). Our maps reveal a double morphology in the E-W direction, on a scale of ~1 kpc, in which both the components

have steep spectra. The low (0.6) concentration index of the core (East) component suggests that additional optically-thin, steep spectrum jet components may hide in the kpc-component and significantly contribute at these frequencies.

NGC1142 It is part of the system *Arp118*, comprising also the spheroidal galaxy NGC1143 (separation ~40 arcsec), and it is most probably the result of a collisional encounter (e.g. Joy & Ghigo 1988). The system presents a morphology with a southern ridge of radio emission, corresponding to optical emission line knots, a compact component close to the optical position and a group of three compact components (further resolved into 6) ~8 arcsec far in the NE direction (e.g. Joy & Ghigo 1988; Condon et al. 1990), both having flat spectra (Thean et al. 2000). The triple system has been further by Thean et al. (2001) into 6 components with MER-LIN observations. Our radio maps reveal a complex radio morphology, in which the southern ring of radio emission is visible in the 22 GHz maps, but not in the 45 GHz map. We detect 6 components in the 22 GHz map, but only three are detected also in the naturally-weighted, tapered 45 GHz maps. The morphology of radio emission is similar to previous works at similar resolution (e.g. Thean et al. 2000), but we detect (with high significance) an additional component with respect to previous VLA studies, i.e. component C, only detected at 22 GHz. Only the components A1, A2 and B (where the nucleus is believed to reside) are detected at both bands. The spectral indices for A1 and A2 are steep, while the spectral index for component B is flatter (although borderline, α ~ =0.5±0.13). The separation between the core component and the A1/2 double is ~8 arcsec, corresponding to ~4.5 kpc.

NGC4388 It is a Sy2 edge-on galaxy in the *Virgo* cluster, and it is known for having wide ionisation cones extending well above and below the stellar disk (e.g. Ayani & Iye 1989). VLA observations reveal a cross-like morphology extending for in the N direction ~19 arcsec (P.A. ~10 deg), with a central double of ~1.9 arcsec, constituted by a southern component which may be associated to a spike in optical emission lines (e.g. Hummel & Saikia 1991; Falcke et al. 1998; Ho & Ulvestad 2001; Damas-Segovia et al. 2016) and a northern component forming a collimated jet (e.g. Kukula et al. 1999; Mundell et al. 2000). The nucleus is detected by Giroletti & Panessa (2009) with EVN only at 1.6 GHz, with a T_B ~10^6 K, which can not rule out a thermal origin. Smith et al. (2016) studied it with VLA in C configuration at 22 GHz (~1 arcsec resolution), finding an elongated morphology, but no double component, with flux density ~3.26 mJy. Behar et al. (2018) observed it with CARMA at 100 GHz reporting flux density of 3.58±0.34 mJy. Our radio maps reveal a double morphology in the direction NE-SW, with a ridge of radio emission between the components which are ~1.9 arcsec apart (~330 pc). The spectral slope of the northern component (where the nucleus is believed to reside) is flat (α =0.27±0.11) while the southern component exhibits a steeper spectrum (α =0.87±0.09). The position quoted by Smith et al. (2016) is compatible with our northern component, and the flux density of our northern component is compatible with both their 22 GHz flux and the 100 GHz flux of Behar et al. (2018), the same being valid for the high-frequency spectral slope.

NGC1068 It is a well studied Seyfert 2 galaxy, which is

know to have bipolar NLR outflowing structures apparently aligned with the radio jet (e.g. Crenshaw et al. 2000; Whittle et al. 2005). We keep the nomenclature of Wilson & Ulvestad (1983), for previous VLA and VLBI maps see (e.g. Wilson & Willis 1980; Wilson 1981; van der Hulst et al. 1982; Wilson & Ulvestad 1982; Kukula et al. 1995b). The Wilson & Ulvestad (1983) maps at 4.9 and 15 GHz (~0.4 arcsec resolution) reveal four components aligned in the NE-SW direction on a scale of ~13 arcsec, interpreted as a radio jet emanating from the nucleus, which is resolved into three structure. The steep-spectrum NE lobe is find to be coincident with the edge of the optical line emitting clouds. High resolution observations (e.g. Pedlar et al. 1983; Ulvestad et al. 1987; Taylor et al. 1996b) resolved the central component into several components constituting a jet. However, in a series of paper, Gallimore et al. performed high resolution observations on the central component of the source concluding that the component having the flattest spectrum has a low T_B ~ 3×10^5 K brightness temperature, which would favour a thermal bremsstrahlung emission from inner edge of a torus instead of synchrotron self-absorption from the base of a jet (e.g. Gallimore et al. 1996a,b, 2004), but see also Roy et al. (1998); Cotton et al. (2008). Our radio maps reveal a morphology compatible with previous VLA observations at comparable resolution, with an overall extension in the SE-NW direction of ~16 arcsec (~1.3 kpc). The (a) component presents flux densities of 151 - 83 mJyand a steep spectral index (α =+0.88±0.11), in agreement with previous works. The component (b), where high-resolution observations have identified the nucleus, the flux densities are in the range 129 - 72 mJywith a spectral index α =+0.85±0.10, again compatible with previous works at similar resolution. The component (c) in Wilson & Ulvestad (1983) is only seen at 22 GHz with flux density TOT mJy. The extended component in the SW (not considered in Wilson & Ulvestad 1983) exhibit a flatter spectrum (α =0.47±0.14) and flux densities of 16 - 12 mJy .

This paper has been typeset from a TEX/LATEX file prepared by the author.
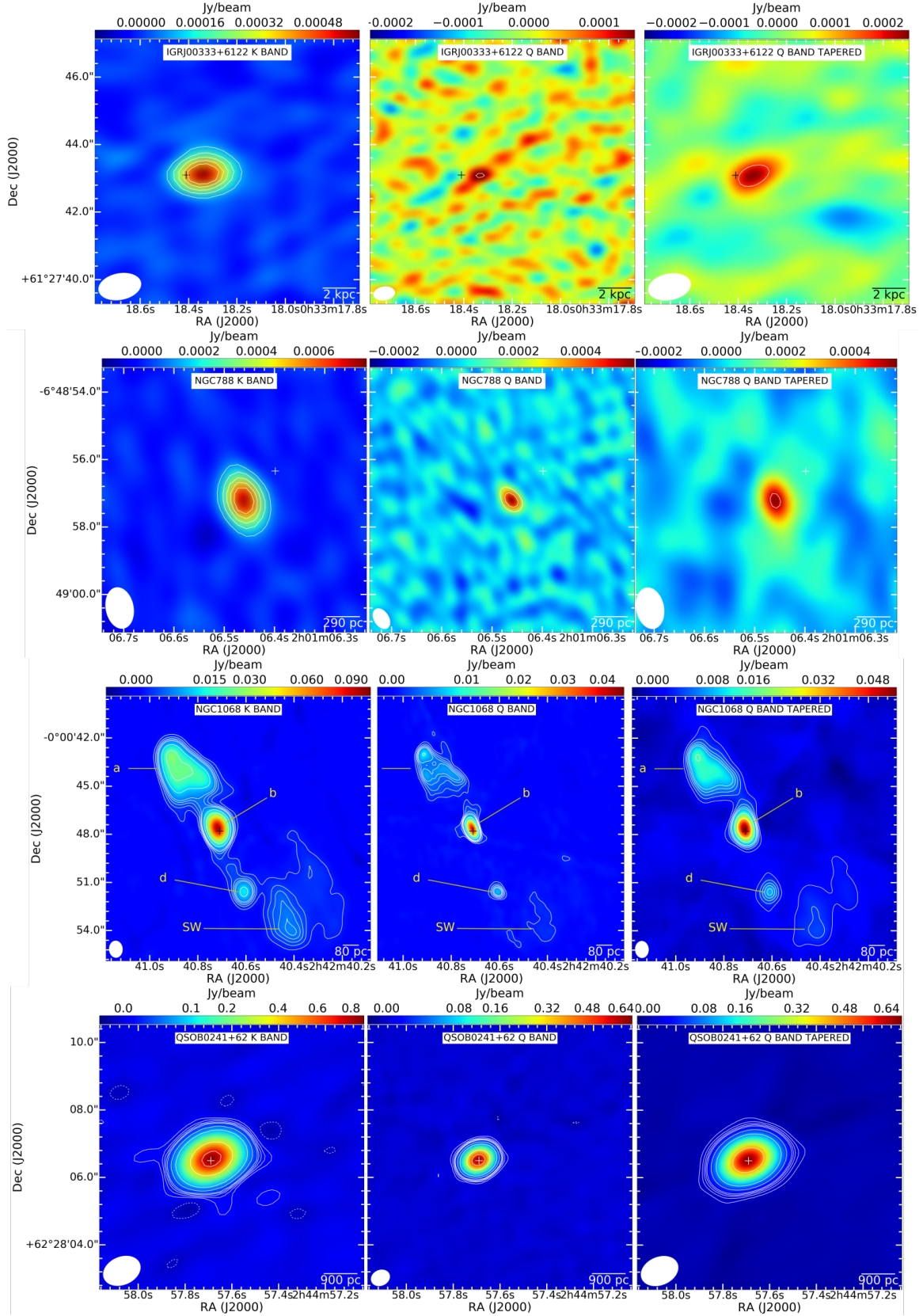
Figure A1. Contour and coloured maps for IGRJ00333+6122, NGC788, NGC1068 and QSOB0241+62 (from top to bottom). For each source we show the map at the K band (left), at Q band (centre) and at Q band after tapering and natural weighting (right). The contours are shown at the [-5,5,10,15,20,25,50,100,500,1000,5000] × σ_{image}, using the image RMS reported in Table A1. The horizontal bar in the bottom-right corner of each panel represents the linear scale corresponding to 1 arcsec. The cross corresponds to the position quoted in Table A1.
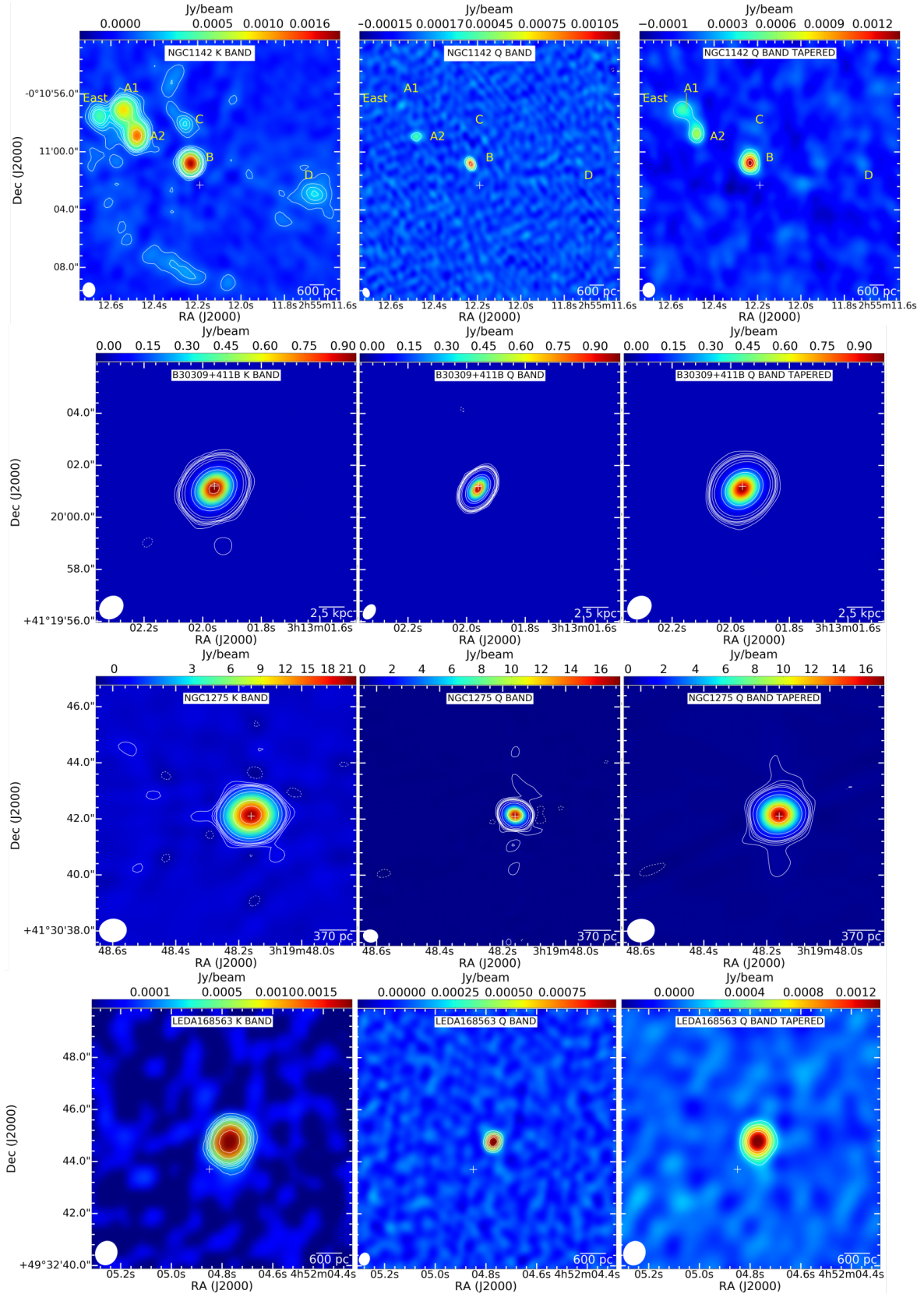
Figure A2. Contour and coloured maps for NGC1142, B30309+411B, NGC1275 and LEDA168563 (from top to bottom). For each source we show the map at the K band (left), at Q band (centre) and at Q band after tapering and natural weighting (right). The contours are shown at the [-5,5,10,15,20,25,50,100,500,1000,5000] × σ_{image}, using the image RMS reported in table Table A1. The horizontal bar in the bottom-right corner of each panel represents the linear scale corresponding to 1 arcsec. The cross corresponds to the position quoted in Table A1.
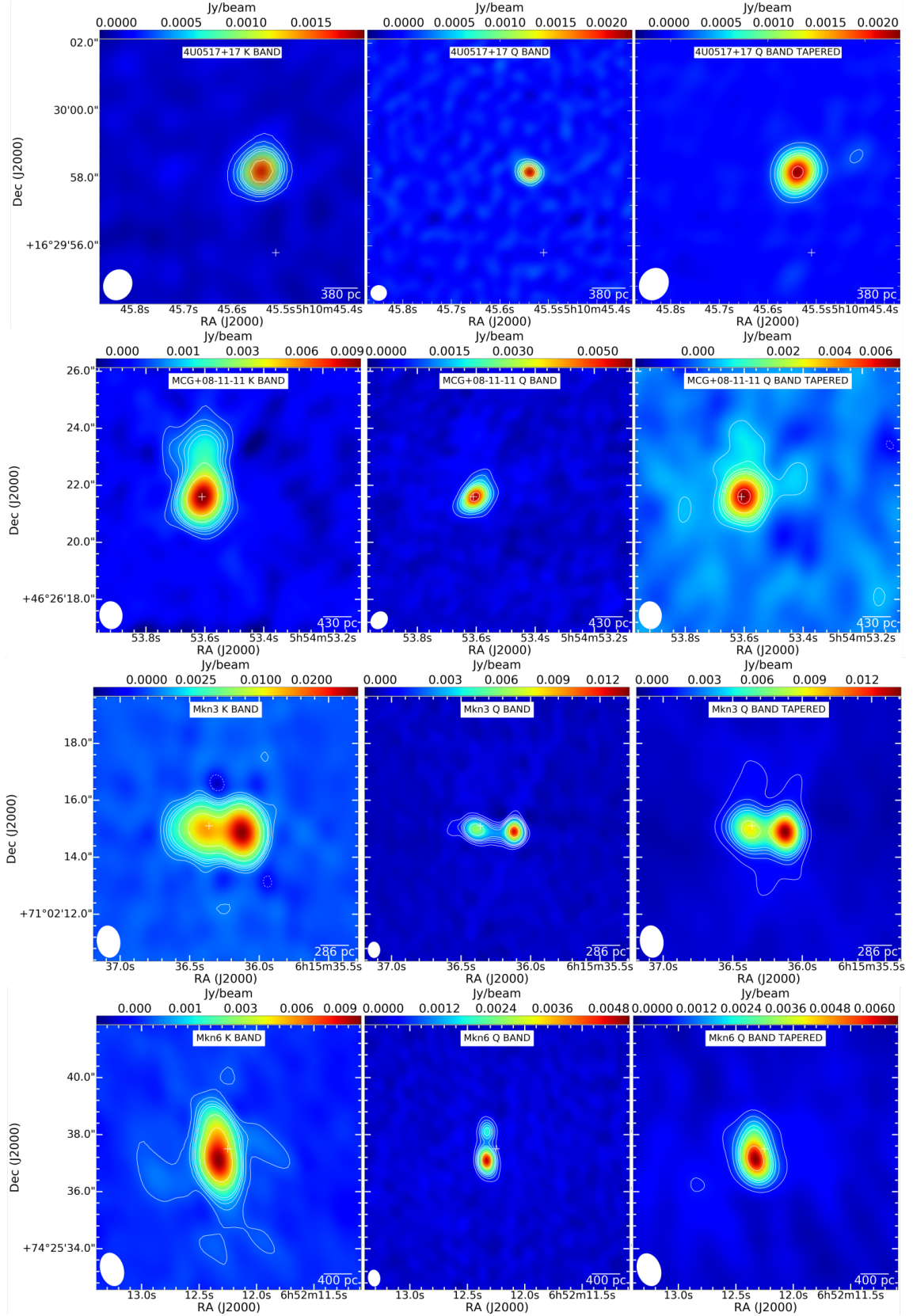
Figure A3. Contour and coloured maps for 4U0517+17, MCG+08-11-11, Mkn3 and Mkn6 (from top to bottom). For each source we show the map at the K band (left), at Q band (centre) and at Q band after tapering and natural weighting (right). The contours are shown at the $[-5,5,10,15,20,25,50,100,500,1000,5000] \times \sigma_{image}$, using the image RMS reported in table Table A1. The horizontal bar in the bottom-right corner of each panel represents the linear scale corresponding to 1 arcsec. The cross corresponds to the position quoted in Table A1.
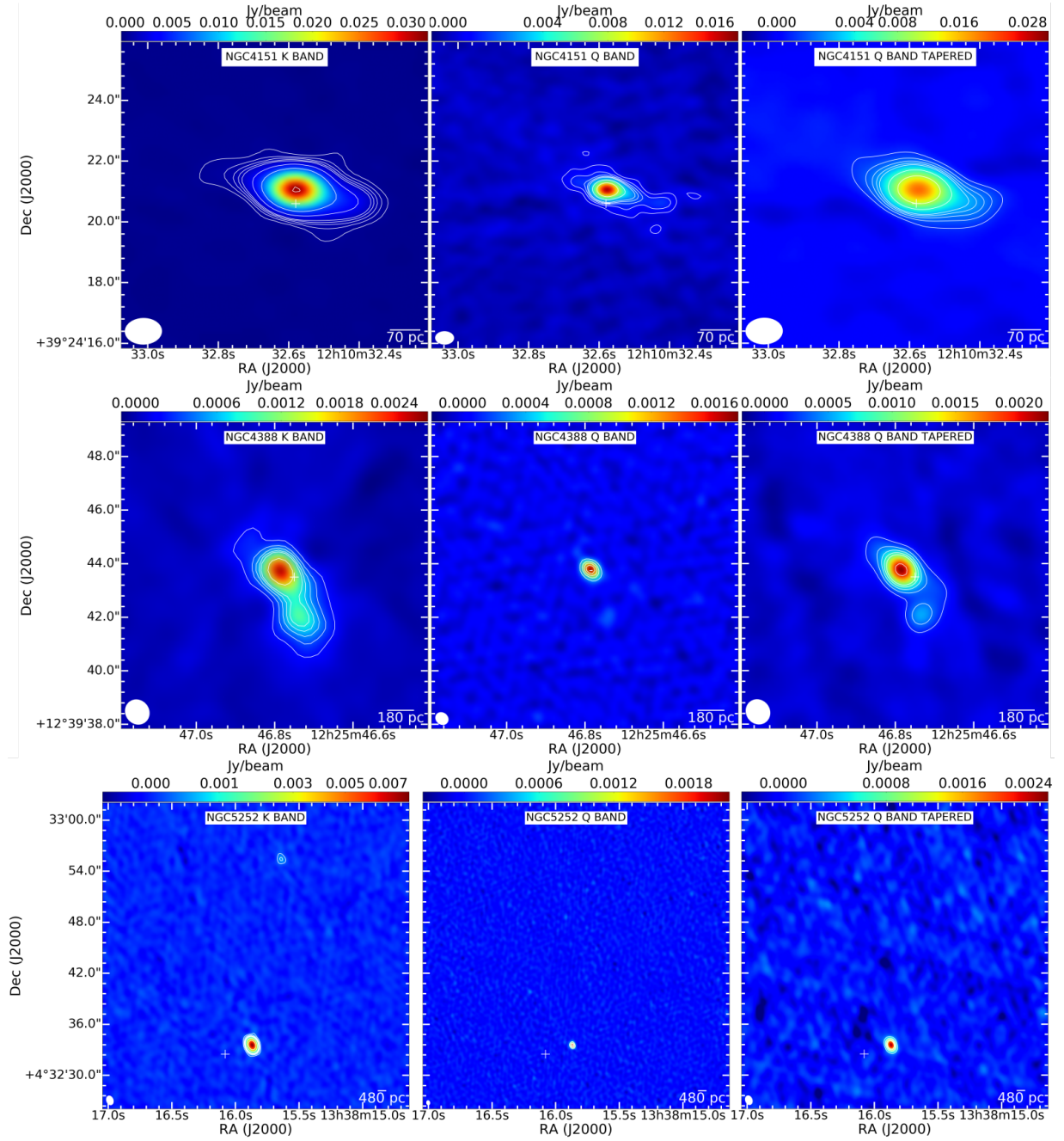
Figure A4. Contour and coloured maps for NGC4151, NGC4388 and NGC5252 (from top to bottom). For each source we show the map at the K band (left), at Q band (centre) and at Q band after tapering and natural weighting (right). The contours are shown at the $[-5,5,10,15,20,25,50,100,500,1000,5000] \times \sigma_{image}$, using the image RMS reported in table Table A1. The horizontal bar in the bottom-right corner of each panel represents the linear scale corresponding to 1 arcsec. The cross corresponds to the position quoted in Table A1.

Table A1: Imaging results for the sources in our sample. *Columns:* (1) Target name; (2) Frequency band; (3) Image noise rms [μJy beam^{-1}], unless specified; (4) Component (only for the resolved sources); (5) Integrated flux density (mJy); (6) Peak intensity (mJy beam^{-1}); (7) Deconvolved FWHM dimensions (major × minor axis) for the fitted source, determined from an elliptical Gaussian fit source size (milliarcsec); (8) Source position angle (deg); (9) & (10) Detected source position in epoch J2000 (hh:mm:ss and ^{o}:$'$:$''$); (11) Spectral index calculated from the 22 GHz and the 45 GHz naturally-weighted, tapered maps. For NGC5252 only the spectral index of the southern (core) component is shown as the northern component is not associated with the AGN (see following sections).

Target (1)	Band (2)	σ_{image} (3)	Component (4)	F$_{total}$ (5)	F$_{peak}$ (6)	$\theta_M \times \theta_m$ (7)	P.A. (8)	α_{J2000} (9)	δ_{J2000} (10)	α (11)
NGC788	K	24		0.87±0.06	0.80±0.05	<0.6 × 0.4	⋯	02:01:06.46±0.01	-06.48.57.22±0.02	+0.4±0.25
	Q	41		0.62±0.05	0.56±0.07	<0.3 × 0.2	⋯	02:01:06.46±0.015	-06.48.57.20±0.02	
	Q-tapered	44		0.66±0.10	0.50±0.05	(930±350) × (270±180)	180±30	02:01:06.45±0.03	-06.48.57.30±0.07	
4U0517+17	K	26		2.08±0.12	1.9±0.10	(300±60) × (200±150)	80±60	05:10:45.540±0.005	+16.29.58.214±0.006	-0.09±0.11
	Q	62		2.42±0.16	2.31±0.13	<0.2 × 0.2	⋯	05:10:45.539±0.006	+16.29.58.182±0.005	
	Q-tapered	38		2.23±0.13	2.19±0.13	<0.5 × 0.4	⋯	05:10:45.538±0.006	+16.29.58.180±0.007	
IGRJ00333+6122	K	17		0.70±0.05	0.62±0.04	<0.6 × 0.4	⋯	00:33:18.34±0.02	+61.27.43.13±0.01	+1.2±0.4
	Q	38		0.32±0.09	0.17±0.03	<0.3 × 0.2	⋯	00:33:18.33±0.13	+61.27.43.1±0.1	
	Q-tapered	36		0.29±0.07	0.25±0.07	<0.6 × 0.4	⋯	00:33:18.33±0.09	+61.27.43.11±0.05	
B30309+411B	K	181		1.05±0.05 Jy	1.05±0.05 Jy/beam	(45±4) × (30±10)	19±17	03:13:01.960±0.005	+41.20.01.100±0.004	+0.06±0.1
	Q	157		1.01±0.05 Jy	1.00±0.05 Jy/beam	(52±2) × (28±2)	130±3	03:13:01.961±0.004	+41.20.01.097±0.006	
	Q-tapered	260		1.01±0.05 Jy	1.01±0.05 Jy/beam	<0.5 × 0.4	⋯	03:13:01.960±0.006	+41.20.01.097±0.005	
LEDA168563	K	17		3.19±0.16	3.0±0.15	(245±30) × (190±40)	⋯	04:52:04.770±0.004	+49.32.44.759±0.005	+1.07±0.12
	Q	40		1.6±0.1	1.45±0.08	(160±50) × (50±90)	⋯	04:52:04.771±0.005	+49.32.44.764±0.006	
	Q-tapered	38		1.6±0.1	1.56±0.09	<0.5 × 0.4	⋯	04:52:04.770±0.005	+49.32.44.767±0.007	
NGC4151	K	63		43.5±2.2	31.0±1.5	(1060±6) × (258±7)	76.0±0.3	12:10:32.575±0.005	+39.24.21.050±0.006	+0.7±0.1
	Q	86		22.6±1.15	16.2±0.8	(500±9) × (174±7)	78±1	12:10:32.575±0.004	+39.24.21.047±0.006	
	Q - tapered	102		26.2±1.3	19.4±0.9	(980±20) × (240±20)	72±2	12:10:32.572±0.006	+39.24.21.041±0.005	
IGRJ16426+6536	K	8	⋯	<0.024	⋯	⋯	⋯	⋯		
	Q	54	⋯	<0.162	⋯	⋯	⋯	⋯		
QSOB0241+62	K	740		902±45	895±45	(102±13) × (50±30)	63±15	02:44:57.687±0.004	+62.28.06.549±0.005	+0.3±0.1
	Q	505		706±35	702±35	(48±6) × (13±16)	175±12	02:44:57.692±0.005	+62.28.06.513±0.004	
	Q - tapered	872		706±35	701±35	(100±20) × (50±30)	60±30	02:44:57.690±0.005	+62.28.06.518±0.006	
NGC1275	K	14 mJy beam^{-1}		23.0±1.1 Jy	22.9±1.1 Jy beam^{-1}	(80±10) × (52±20)	57±20	03:19:48.161±0.004	+41.30.42.131±0.005	+0.4±0.1
	Q	17 mJy beam^{-1}		17.7±0.9 Jy	17.7±0.9 Jy beam^{-1}	<0.3 × 0.2	⋯	03:19:48.160±0.007	+41.30.42.140±0.006	
	Q - tapered	25 mJy beam^{-1}		17.5±0.9 Jy	17.4±0.9 Jy beam^{-1}	<0.5 × 0.4	⋯	03:19:48.161±0.006	+41.30.42.153±0.007	
Mkn6	K	46		16.6±0.8	10.3±0.5	(1360±14) × (250±14)	1.9±0.3	06:52:12.331±0.005	+74.25.37.245±0.004	+0.8±0.1
	Q (south)	64		6.7±0.4	5.0±0.3	(440±20)×(160±15)	5±2	06:52:12.330±0.005	+74.25.37.086±0.005	
	Q (north)			2.25±0.2	1.9±0.1	(330±65)×(140±105)	170±20	06:52:12.328±0.005	+74.25.38.09±0.01	
	Q-tapered	100		9.7±0.5	6.2±0.3	(1000±50) × (500±40)	⋯	06:52:12.329±0.006	+74.25.37.24±0.01	
NGC5252	K	41	Core	8.8±0.4	8.15±0.4	(310±30) × (225±25)	⋯	13:38:15.869±0.004	+04.32.33.54±0.02	+1.7±0.1
	K		North	0.6±0.1	0.44±0.04	(850±350) × (245±210)	⋯	13:38:15.64±0.03	+04.32.55.42±0.07	
	Q	100	Core	2.35±0.2	2.2±0.15	(164±100) × (50±110)	⋯	13:38:15.868±0.008	+04.32.33.52±0.02	
	Q		North	⋯	<0.3	⋯	⋯	⋯	⋯	
	Q - tapered	62	Core	2.7±0.2	2.5±0.14	(370±160) × (240±130)	⋯	13:38:15.871±0.009	+04.32.33.55±0.01	
	Q - tapered		North	⋯	<0.2	⋯	⋯	⋯	⋯	
Mkn3	K	80	W	34±4	31.7±1.6	(275±14) × (220±20)	130±13	06:15:36.120±0.007	+71.02.14.875±0.005	+1.2±0.1
			E	25.7±0.8	15.3±0.8	(1080±13) × (250±40)	70±1	06:15:36.382±0.005	+71.02.14.947±0.006	+0.87±0.09
	Q	86	W	14.6±0.7	12.5±0.7	(243±9) × (90±44)	99±5	06:15:36.119±0.005	+71.02.14.894±0.004	
			E	12.7±0.7	6.0±0.3	<0.3 < 0.2	⋯	06:15:36.375±0.007	+71.02.14.956±0.006	
	Q-tapered	150	W	15.1±0.8	13.6±0.7	(424±50) × (210±70)	170±12	06:15:36.117±0.006	+71.02.14.883±0.007	
			E	14.1±0.8	8.6±0.5	(900±55) × (560±80)	67±8	06:15:36.375±0.009	+71.02.14.97±0.01	
NGC4388	K	32	NE	3.5±0.2	2.6±0.1	(700±30) × (370±35)	52±4	12:25:46.786±0.006	+12.39.43.732±0.006	+0.27±0.11
			SW	3.1±0.2	0.9±0.05	(1825±95) × (1080±65)	13±4	12:25:46.73±0.02	+12.39.42.13±0.03	+1.6±0.26
	Q	67	NE	2.16±0.2	1.8±0.1	(310±60) × (100±60)	40±16	12:25:46.785±0.009	+12.39.43.774±0.009	
			SW	⋯	⋯	⋯	⋯	⋯	⋯	
	Q-tapered	40	NE	2.9±0.2	2.14±0.1	(784±45) × (270±70)	49±4	12:25:46.786±0.009	+12.39.43.772±0.006	
			SW	1.03±0.14	0.50±0.05	(1520±20) × (480±24)	154±6	12:25:46.72±0.05	+12.39.42.22±0.07	
NGC1142	K	10	East	0.87±0.04	0.34±0.01	(1500±70) × (825±65)	100±4	02:55:12.63±0.02	-00.10.57.526±0.02	
			A1	2.0±0.1	0.93±0.05	(1050±30) × (940±30)	42±14	02:55:12.539±0.005	-00.10.57.182±0.007	+0.9±0.25
			A2	2.25±0.1	1.32±0.07	(1060±20) × (540±30)	13±1	02:55:12.482±0.005	-00.10.58.806±0.006	+1.4±0.3
			B	2.24±0.1	2.1±0.1	(300±15) × (60±60)	84±6	02:55:12.232±0.001	-00.11.00.804±0.005	+0.5±0.13

Table A1: Imaging results for the sources in our sample. *Columns:* (1) Target name; (2) Frequency band; (3) Image noise rms [μJy beam^{-1}], unless specified; (4) Component (only for the resolved sources); (5) Integrated flux density (mJy); (6) Peak intensity (mJy beam^{-1}); (7) Deconvolved FWHM dimensions (major × minor axis) for the fitted source, determined from an elliptical Gaussian fit source size (milliarcsec); (8) Source position angle (deg); (9) & (10) Detected source position in epoch J2000 (hh:mm:ss and ^{o}:$'$:$''$); (11) Spectral index calculated from the 22 GHz and the 45 GHz naturally-weighted, tapered maps. For NGC5252 only the spectral index of the southern (core) component is shown as the northern component is not associated with the AGN (see following sections).

Target (1)	Band (2)	σ_{image} (3)	Component (4)	F_{total} (5)	F_{peak} (6)	$\theta_M \times \theta_m$ (7)	P.A. (8)	α_{J2000} (9)	δ_{J2000} (10)	α (11)
			D	0.71±0.05	0.18±0.01	(1780±140) × (1440±130)	85±20	02:55:11.66±0.05	-00.11.02.89±0.04	
	Q	42	East	⋯	<0.12	⋯	⋯	⋯	⋯	
			A1	0.17±0.06	0.21±0.04	<0.3 × <0.2	⋯	02:55:12.55±0.05	-00.10.56.79±0.05	
			A2	0.5±0.1	0.41±0.05	<0.3 × <0.2	⋯	02:55:12.480±0.004	-00.10.58.93±0.02	
			B	1.2±0.1	1.16±0.07	<0.3 × <0.2	⋯	02:55:12.231±0.007	-00.11.00.82±0.01	
			D	⋯	<0.12	⋯	⋯	⋯	⋯	
	Q-tapered	51	East	⋯	<0.15	⋯	⋯	⋯	⋯	
			A1	1.0±0.2	0.45±0.06	(1360±30) × (780±30)	70±20	02:55:12.54±0.08	-00.10.57.17±0.06	
			A2	0.85±0.2	0.67±0.06	(1380±40) × (490±40)	16±18	02:55:12.48±0.02	-00.10.58.63±0.05	
			B	1.6±0.1	1.4±0.1	(470±130) × (290±190)	17±82	02:55:12.24±0.014	-00.11.00.72±0.02	
			D	⋯	<0.153	⋯	⋯	⋯	⋯	
NGC1068	K	208	a	151.7±7.7	⋯	2700×1500	⋯	⋯	⋯	+0.9±0.1
			b	128.8±6.4	98.8±4.9	(767±6) × (252±8)	23.0±0.5	02:42:40.7185±0.008	-00.00.47.607±0.007	+0.8±0.1
			d	16.2±0.9	12.2±0.7	(620±60) × (460±60)	33±17	02:42:40.609±0.007	-00.00.51.55±0.01	+0.47±0.01
			SW	60.8±3.8	⋯	4200×3100	⋯	⋯	⋯	+0.14±0.13
	Q	160	a	88.6±4.8	⋯	2720×1560	⋯	⋯	⋯	
			b	70.4±3.5	40.4±2.0	(733±6) × (185±5)	19.0±0.3	02:42:40.713±0.009	-00.00.47.635±0.007	
			d	9.2±0.6	6.0±0.4	(420±50) × (308±60)	80±20	02:42:40.607±0.007	-00.00.51.568±0.008	
			SW	57.6±4.8	⋯	5950×3200	⋯	⋯	⋯	
	Q - tapered	295	a	82.7±4.5	⋯	2600×1500	⋯	⋯	⋯	
			b	71.9±3.7	54.9±2.8	(810±15) × (220±20)	14±1	02:42:40.714±0.005	-00.00.47.615±0.006	
			d	12.0±1.0	7.3±0.5	(900±100) × (600±100)	170±20	02:42:40.612±0.02	-00.00.51.58±0.03	
			SW	55.3±3.4	⋯	6100×3000	⋯	⋯	⋯	
MCG+08-11-11	K	40	core	15.6±0.8	10.2±0.5	(840±10) × (440±10)	160±1	05:54:53.607±0.006	+46.26.21.617±0.004	+0.7±0.1
			jet	2.8±0.8	⋯	⋯	⋯	⋯	⋯	+1.1±0.4
			total	18.8±1.2	⋯	⋯	⋯	⋯	⋯	+0.79±0.14
	Q	98	core	9.4±0.5	5.4±0.3	(70±30) × (400±2)	140±4	05:54:53.602±0.007	+46.26.21.595±0.007	
	Q-tapered	116	core	9.3±0.5	7.1±0.4	(570±50) × (390±80)	130±20	05:54:53.600±0.006	+46.26.21.609±0.008	
			jet	1.3±0.1	⋯	⋯	⋯	⋯	⋯	
			total	10.9±0.8	⋯	⋯	⋯	⋯	⋯	